



Fibroblastic reticular cell lineage convergence in Peyer's patches governs intestinal immunity

Alejandro Prados^{1,5}, Lucas Onder^{2,5}, Hung-Wei Cheng², Urs Mörbe², Mechthild Lütge², Cristina Gil-Cruz², Christian Perez-Shibayama², Vasiliki Koliaraki¹, Burkhard Ludewig^{2,3,6} and George Kollias^{1,4,6}

Fibroblastic reticular cells (FRCs) determine the organization of lymphoid organs and control immune cell interactions. While the cellular and molecular mechanisms underlying FRC differentiation in lymph nodes and the splenic white pulp have been elaborated to some extent, in Peyer's patches (PPs) they remain elusive. Using a combination of single-cell transcriptomics and cell fate mapping in advanced mouse models, we found that PP formation in the mouse embryo is initiated by an expansion of perivascular FRC precursors, followed by FRC differentiation from subepithelial progenitors. Single-cell transcriptomics and cell fate mapping confirmed the convergence of perivascular and subepithelial FRC lineages. Furthermore, lineage-specific loss- and gain-of-function approaches revealed that the two FRC lineages synergistically direct PP organization, maintain intestinal microbiome homeostasis and control anticoronavirus immune responses in the gut. Collectively, this study reveals a distinct mosaic patterning program that generates key stromal cell infrastructures for the control of intestinal immunity.

Tight regulation of intestinal immune responses is critical for the maintenance of epithelial cell functions to prevent severe diseases, such as inflammatory bowel disease¹ or colorectal cancer². Immune cell trafficking and pathogenic cytokine circuits are critical drivers in both intestinal inflammation and cancer progression³. The initiation, sustenance and regulation of such immune processes occur in gut-associated lymphoid tissues, including Peyer's patches and mesenteric lymph nodes (LNs)⁴. The subepithelial location of PPs provides direct access to intestinal antigens for immune cells, leading to the production of vast amounts of protective immunoglobulin A (IgA)⁵. Distinct topological niches for immune cell activation in PPs are constructed by FRCs, which not only provide a structural scaffold and guidance to immune cells⁶, but also shape immune responses through the provision of essential cytokines and growth factors⁷. Podoplanin (PDPN)-expressing FRCs of the T cell zone in lymph nodes (TRCs) regulate the migration and survival of T cells through the production of T cell- and dendritic cell-attracting chemokines CCL19 and CCL21 (refs. ^{8,9}). Reticular cells located at the border between the T and B cell zones (TBRCs) in PPs control group 1 innate lymphoid cell (ILC) activity through production of interleukin-15 (IL-15)⁷. Follicular dendritic cells (FDCs), together with TBRCs, cater to B cells and thereby foster antibody production through the organization of the germinal center (GC)^{10,11}. While recent studies have provided insight into FRC differentiation programs in LNs and the splenic white pulp^{10–14}, the origin and differentiation trajectories of PP FRCs have remained unexplored.

Secondary lymphoid organ development depends on the interaction of hematopoietic lymphoid tissue inducer (LTi) cells with resident mesenchymal and endothelial lymphoid tissue organizer (LTo) cells^{15–17}. PP organogenesis is initiated at embryonic day (E) 16.5, when LTi cells form clusters along the intestinal wall and induce the

differentiation of LTo cells^{18,19}. This process requires lymphotoxin- β receptor (LT β R)-dependent activation of mesenchymal LTo cells^{9,20}. During the first week of life, T and B lymphocytes seed the PP primordium, accumulate in proximity to the muscular layer²¹ and drive the development of distinct FRC niches^{22,23}. Here, we show that PP FRCs develop from two separate mesenchymal LTo cell lineages. Perivascular and subepithelial PP FRC lineages converge and form mosaic microenvironments in an LT β R- and tumor necrosis factor receptor (TNFR) 1-dependent manner. The cooperation of the two FRC lineages in PPs is crucial for the maintenance of intestinal homeostasis and the induction of anticoronavirus IgA responses.

Results

Molecular definition of the PP FRC landscape. PPs are underpinned by a dense network of FRCs (Fig. 1a). To elaborate the subset composition and topological organization of PP FRCs, we employed well-characterized *Ccl19*^{Cre} (ref. ⁹) and *Col6a1*^{Cre} (ref. ²⁴) mouse models that permit FRC targeting in secondary lymphoid organs. While FRC networks in PPs were highlighted to different extents when the respective Cre-driver lines were crossed with an enhanced yellow fluorescent protein (EYFP) reporter strain (Fig. 1b), the combination of both lines resulted in targeting of all PP FRCs (Fig. 1b and Extended Data Fig. 1a–c). To define PP FRC subsets and their relation to the observed FRC lineages, we isolated fibroblasts from *Col6a1*^{EYFP} and *Ccl19*^{EYFP} PPs (Extended Data Fig. 2a,b) and performed droplet-based single-cell transcriptomics analysis. In total, 9,719 vascular cell adhesion protein 1 (VCAM1)- and/or PDPN-positive fibroblasts were profiled, which contained 4,492 EYFP-expressing fibroblasts originating from either of the two transgenic lines (Extended Data Fig. 2c). Clustering analysis of EYFP-expressing fibroblasts and mapping based on *Adamde1*, *Bmp5* or *Clu* expression^{25,26} discriminated six *Clu*-expressing PP

¹Institute for Bioinnovation, BSRC "Alexander Fleming", Vari, Greece. ²Institute of Immunobiology, Kantonsspital St Gallen, St Gallen, Switzerland.

³Institute of Experimental Immunology, University of Zürich, Zürich, Switzerland. ⁴Department of Physiology, Medical School, National and Kapodistrian University of Athens, Athens, Greece. ⁵These authors contributed equally: Alejandro Prados, Lucas Onder. ⁶These authors jointly supervised this work: Burkhard Ludewig, George Kollias. ✉e-mail: burkhard.ludewig@kssg.ch; kollias@fleming.gr

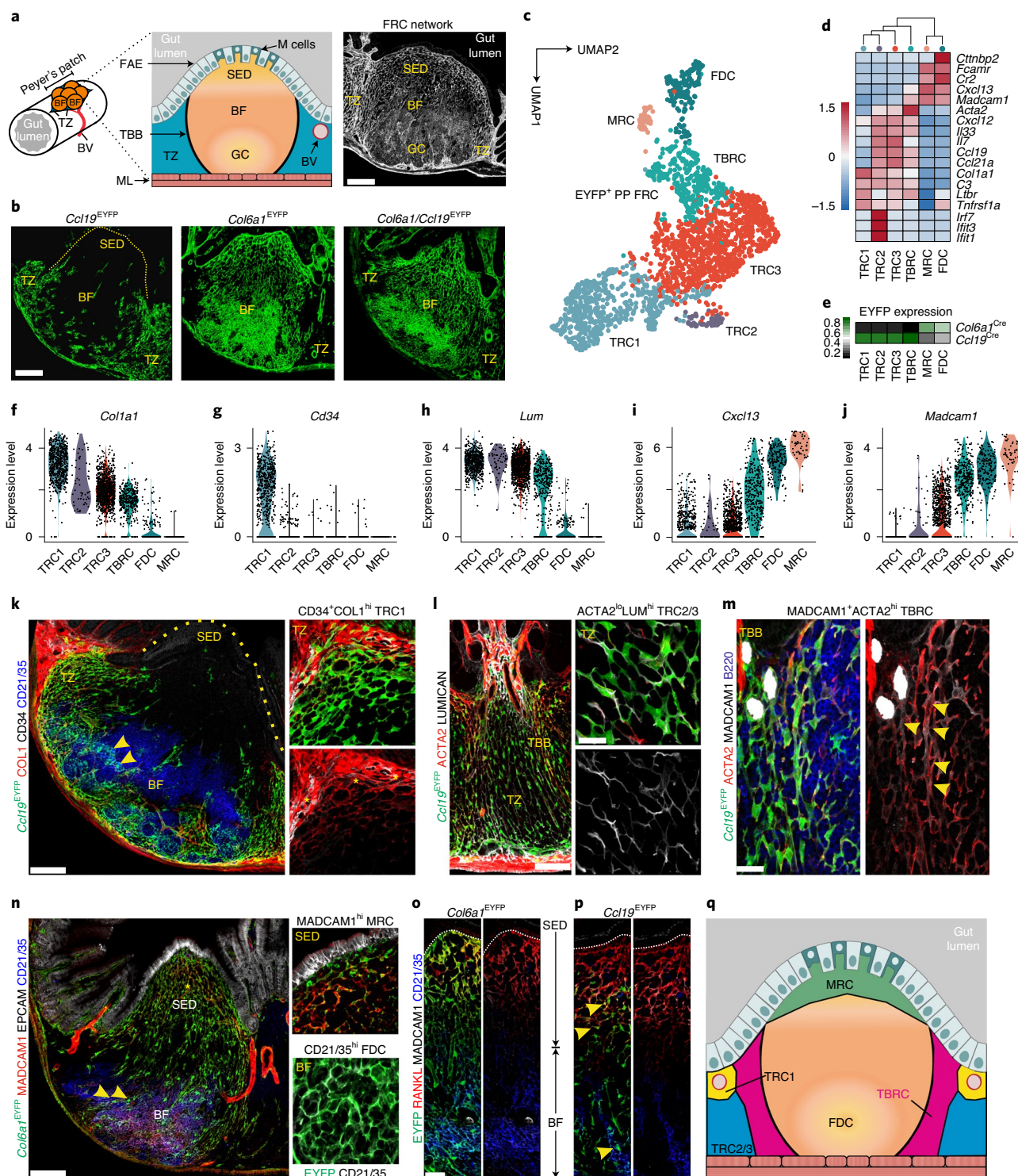


Fig. 1 | The FRC landscape of Peyer's patches. **a**, Murine PPs consist of large B cell follicles (BF) and interfollicular T cell zones (TZ), demarcated from the gut lumen through the FAE with M cells and underpinned by a PDPN⁺VCAM1⁺ FRC network; BV, blood vessel; GC, germinal center; SED, subepithelial dome; TBB, T-B cell zone border. **b**, Confocal microscopy of EYFP⁺ FRC networks in PPs of 6-week-old transgenic mice. **c**, UMAP analysis of EYFP⁺ PP FRCs from adult *Ccl19*^{EYFP} and *Col6a1*^{EYFP} mice. **d**, Hierarchical clustering of averaged expression of canonical FRC marker genes. **e**, Heat map showing averaged EYFP expression in FRC clusters of the indicated lineages. **f–j**, Violin plots depicting subset-specific expression of the indicated genes in single FRCs: *Col1a1* (**f**), *Cd34* (**g**), *Lum* (**h**), *Cxcl13* (**i**), *Madcam1* (**j**). **k**, Confocal microscopy analysis of BF and SED in PPs of adult *Ccl19*^{EYFP} mice. Arrowheads indicate EYFP⁺CD21/35⁺ FDCs. Asterisks indicate CD34^{hi}COL1^{hi} TRCs. **l**, Confocal microscopy analysis of the TZ and TBB in PPs of adult *Ccl19*^{EYFP} mice. **m**, FRC network in the TBB, arrowheads indicate ACTA2^{hi}MADCAM1⁺ TBRCs. **n**, Confocal microscopy analysis of BF and SED in PPs of adult *Col6a1*^{EYFP} mice. Higher magnification images on the right show EYFP⁺MADCAM1⁺ MRC in the SED and EYFP⁺CD21/35⁺ FDC networks in the BF. **o,p**, Confocal microscopy analysis of FRC networks spanning from the SED to BF. Arrowheads show EYFP⁺ FDCs and MRCs in *Ccl19*^{EYFP} mice. **q**, Schematic depiction of FRC subset location in the PP. Scale bars, 200 μm (**a,b,k,n**); 100 μm (**l**); 20 μm (**m**); 10 μm (**l,o,p**). Images are representative of 3–5 mice per group and at least two independent experiments. scRNA-sequencing data represent 2,220 EYFP⁺ FRCs, *n* = 8 biological replicates, four independent experiments.

FRC populations from *Adamdec1*-expressing lamina propria fibroblasts and *Bmp5*-expressing subepithelial fibroblasts (Extended Data Fig. 2d–f). Re-analysis of the six FRC clusters and evaluation of cluster-specific gene expression identified three T cell zone reticular cell subsets (TRC1–3) and TBRCs, while FDCs and marginal zone reticular cells (MRCs) formed individual clusters (Fig. 1c,d and Extended Data Fig. 2g). Distribution of EYFP messenger RNA expression among FRC clusters (Fig. 1e and Extended Data Fig. 2c) and expression of distinct marker genes (Fig. 1f–j) indicated that the TRC populations belong mainly to a cell lineage targeted by the *Ccl19*^{EYFP} transgene, while FDCs and MRCs originated mainly from a separate *Col6a1*^{EYFP} lineage. High expression of extracellular matrix-associated genes *Col1a1*, *Col3a1*, *Col5a1* and *Col14a1*, and expression of the perivascular reticular cell markers *Cd34* and *Ly6a* (Fig. 1f,g and Extended Data Fig. 2g) in TRC1 were indicative for a perivascular niche localization. High-resolution confocal microscopy of *Ccl19*^{EYFP} PPs confirmed the presence of CD34⁺COL1^{hi} TRC1 in the vicinity of blood vessels of the T cell zone (Fig. 1k). High expression of *Col1a1* and *Lum* (Fig. 1f,h) and other classical TRC marker genes, but a low level of *Acta2* expression (Fig. 1d), identified TRC2 and 3 as bona fide TRCs. TRC2 could be distinguished from TRC3 mainly by the expression of genes related to the interferon system (Fig. 1d and Extended Data Fig. 2g), indicating a switch of TRC3 to an activated state²⁷. High-resolution confocal microscopy of *Ccl19*^{EYFP} PPs confirmed the presence of ACTA2^{lo}LUM^{hi} TRC2/3 in the center of the T cell zone (Fig. 1l). Moderate expression of classical TRC marker genes, but elevated expression of *Acta2* (Fig. 1d), *Cxcl13* and *Madcam1* (Fig. 1i,j), identified the TBRC cluster, and the location of MADCAM1⁺ACTA2^{hi} cells at the T–B border (Fig. 1l,m) is compatible with the designation as TBRC¹⁴. The expression of the canonical MRC and FDC markers CD21/CD35 (complement receptors 2 and 1, respectively) and MADCAM1 was particularly high on EYFP⁺ FRC networks in GCs and the subepithelial dome (SED) of *Col6a1*^{EYFP} PPs (Fig. 1n). Comparative analysis of FRC networks in the subepithelial domes and B cell follicles revealed that the majority of RANKL⁺ MRCs and CD21/35⁺ FDCs belong to the *Col6a1*^{EYFP} lineage (Fig. 1o), whereas a smaller fraction MRCs and FDCs could be identified in the follicle and SED region of *Ccl19*^{EYFP} PPs (Fig. 1k,p, arrowheads). Taken together, the molecular definition of the PP FRC landscape reveals two FRC lineages furnishing distinct microenvironmental niches (Fig. 1q).

Lineage convergence of PP FRCs. To further elaborate the relationship and differentiation trajectories of the *Ccl19*^{Cre} and *Col6a1*^{Cre} PP FRC lineages, we computed differentiation trajectories on the basis of the single-cell transcriptomics data from PP FRCs using the Monocle routine²⁸. The two FRC lineages contributed to two distinct trajectories, with the majority (67.8%) of *Col6a1*^{Cre}-expressing cells forming a MRC–FDC trajectory (T1), while 90.4% of the cells in the TRC trajectory (T2) belonged to the *Ccl19*^{Cre} lineage (Fig. 2a,b). LTβR-dependent FRC maturation marker genes *Ccl19* and *Ccl21a* (ref. 9) were enriched in TRC2/3 and TBRC (Extended Data Fig. 3a), while expression of perivascular reticular cell marker genes, for example, *Ly6a*, *Klf4* and *CD34* (ref. 12), was highest in TRC1 (Extended Data Fig. 3b). The location of *Cxcl13*^{hi}*Madcam1*^{hi} MRC on one end and *Cr2*^{int}*Fcammr*^{int} FDC on the other end of T1 (Extended Data Fig. 3c,d) is in line with the proposed developmental relationship between FDCs and MRCs¹⁴. To validate the in silico-predicted differentiation trajectories of the two FRC lineages, we first traced the origin and expansion of *Ccl19*^{Cre} and *Col6a1*^{Cre} LTo cells from E18.5 onwards. Early PP anlagen were identified by the presence of CD3⁺CD4⁺ LTi cell aggregates (Extended Data Fig. 3e). At this stage, *Ccl19*^{Cre}+ER-TR7⁺ cells were found in direct contact with CD31⁺ endothelial cells (Fig. 2c, arrows). In contrast, E18.5 *Col6a1*^{Cre} LTo cells were found adjacent to the epithelial layer

(Fig. 2d, arrow). During the first week after birth, *Ccl19*^{Cre}-expressing LTo cells increased in number along with the expansion of the anlagen and remained in the developing T cell area (Fig. 2c and Extended Data Fig. 3e), while *Col6a1*^{Cre} cells started to form reticular cell networks underpinning the B cell zone (Fig. 2d and Extended Data Fig. 3e). The expansion of both *Ccl19*^{Cre} and *Col6a1*^{Cre} networks did not depend on the presence of T and B lymphocytes, as shown in *Rag*^{-/-} mice (Extended Data Fig. 3f) indicating that contact with LTi cells is sufficient to trigger the activation of either LTo cell subset. Cell fate mapping using the *R26*^{Brainbow2.1} reporter²⁹ crossed to inducible FRC-specific *Ccl19*^{Tta} mice¹² (Extended Data Fig. 4a), hereafter named *Ccl19*^{Bbw2.1}, facilitated tracking of multicolor reporter gene expression and clonal expansion of LTo cells in PP anlagen (Fig. 2e and Extended Data Fig. 4b). Detection of fate-mapped progeny derived from E18.5 LTo cells in P1 and P4 PP anlagen revealed that *Ccl19*-expressing perivascular (p)LTo cells clonally expanded along the growing vasculature (Extended Data Fig. 4c,d). Fate-mapped progeny started to form single-colored networks in the developing T cell zone of P7 PPs (Fig. 2f and Extended Data Fig. 4e). The T cell zones of adult PPs were populated by progeny derived from E18.5 LTo cells (Fig. 2g and Extended Data Fig. 4f,g), including single-colored TRC cohorts, some of which appeared to be connected to blood vessels (Fig. 2h). Furthermore, E18.5 progeny gave rise to cohorts of perivascular TRC1, Lumican (LUM)⁺ TRC2/3 and ACTA2⁺ TBRC (Extended Data Fig. 4h). To validate the predicted differentiation trajectories of *Col6a1*^{Cre} subepithelial (s)LTo cells, we reconstructed whole B cell follicles from adult and developing PPs of *Col6a1*^{Bbw2.1} mice (Fig. 2i and Extended Data Fig. 4i–k) using light sheet microscopy. We found a random distribution of CFP⁺, YFP⁺ and TOMATO⁺ cells in the subepithelial layer directly under the follicle-associated epithelium (FAE) (Fig. 2j, arrowheads). In contrast, single-colored network columns extended from below the subepithelial layer through the SED towards FDC networks in PPs from newborn and adult mice (Fig. 2j and Extended Data Fig. 4i–k), indicating that sLTo cells clonally expand to form mainly MRC and FDC networks in the B cell follicles. Collectively, these data reveal that the progeny of distinct perivascular and subepithelial LTo cell populations converge to shape the PP FRC landscape.

Molecular circuits regulating FRC lineage convergence. To further dissect the molecular mechanisms underlying FRC lineage convergence in PPs, we genetically ablated two key molecular differentiation pathways in *Ccl19*^{Cre} and/or *Col6a1*^{Cre} mice, that is, the LTβR and the TNFR1 signaling pathways. Deletion of *Ltbr* expression in *Ccl19*^{Cre}, but not *Col6a1*^{Cre}, mice led to a significant reduction in PP numbers (Fig. 3a). On the contrary, *Ccl19*^{Cre} and *Col6a1*^{Cre} FRC lineages synergistically contributed to follicle compartmentalization (Fig. 3b) and determined B cell cellularity in PPs (Extended Data Fig. 5a). FRC lineage differentiation was compromised in *Ccl19*^{EYFP}*Ltbr*^{fl/fl} PPs with EYFP⁺ cells exhibiting elevated expression of CD34 and COL1 (Fig. 3c and Extended Data Fig. 5b), reduced CCL21 expression and elevated extracellular matrix deposition (Fig. 3d and Extended Data Fig. 5c) in comparison to *Ltbr*-competent FRCs. When we followed the fate of E18.5 pLTo cells in inducible *Ccl19*^{EYFP}*Ltbr*^{fl/fl} mice to the age of 6 weeks, we found that *Ltbr*-deficient *Ccl19*-expressing FRC progenitors remained arrested in the perivascular TRC1 niche (Fig. 3e, arrowheads). Similarly, ablation of *Ltbr* expression in the *Col6a1*^{Cre} lineage resulted in the lack of transgene-expressing MRC and FDC networks and a remaining subepithelial fibroblast layer covering the SED (Fig. 3f, arrowheads). Moreover, lack of LTβR signaling in either of the lineages led to a maturation defect of lineage-derived FDCs, demonstrated by the lack of CD21/35 expression on *Ccl19*^{EYFP} or *Col6a1*^{EYFP} cells in the GC regions (Fig. 3g, arrows). Additionally, lack of LTβR signaling in the *Ccl19*^{Cre} lineage resulted in the lack of lineage-associated MRCs (Extended Data Fig. 5e). Concomitant ablation of *Ltbr*

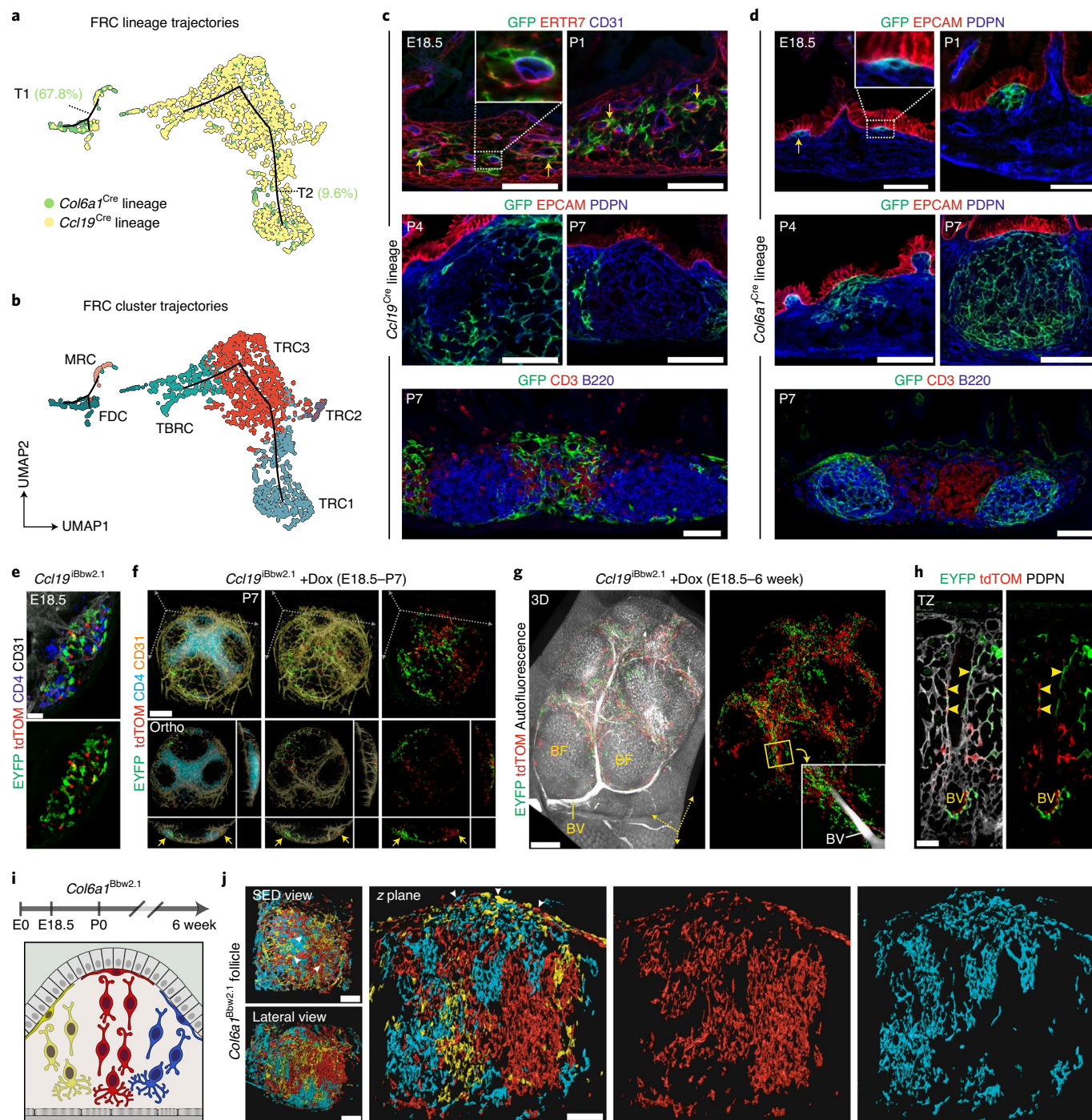


Fig. 2 | Organization of PP microdomains by two distinct LTo cell populations. **a**, Monocle-based trajectory analysis of transcriptomics single-cell data, highlighting cells originating from different lineages. Numbers indicate percentage of cells derived from the *Col6a1*^{Cre} lineage on trajectories (T) 1 and 2. **b**, Projection of FRC clusters on Monocle-based trajectories. **c,d**, Confocal microscopy analysis of PP primordia at E18.5, P4 and P7 from *Ccl19*^{GFP} (**c**) and *Col6a1*^{GFP} (**d**) mice. Boxed areas show the perivascular location in **c** and subepithelial location of GFP⁺ cells in **d**. **e**, Confocal microscopy analysis of E18.5 PP anlagen of *Ccl19*^{iBbw2.1} embryos with EYFP and tdTOMATO reporter expression. **f**, Images showing whole-mount analysis of PP at P7, collected from *Ccl19*^{iBbw2.1} pups treated with doxycycline (Dox) since E18.5. Lower panel shows orthogonal x, y and z views of the upper whole-mount analysis. Arrows indicate single-colored cell clusters. **g**, Images showing whole-mount analysis of PP collected from adult *Ccl19*^{iBbw2.1} mice treated with Dox since E18.5. Higher magnification image shows a major blood vessel (BV) surrounded by EYFP⁺ and tdTOMATO⁺ cell clusters in the T cell zone. **h**, Confocal microscopic analysis of EYFP⁺ and tdTOMATO⁺ progeny of E18.5 progenitors in PDPN⁺ TRC network at 6 weeks of age. Arrowheads indicate perivascular EYFP⁺ and tdTOMATO⁺ TRCs. **i**, Schematic depiction of light sheet microscopy analysis. **j**, Light sheet microscopy images of adult *Col6a1*^{iBbw2.1} PP follicle with single-colored cell columns. Scale bars, 50 μm (**c,d,j**), 20 μm (**e,h**), 100 μm (**f**), 500 μm (**g**). Images are representative of at least three mice from 2–4 independent experiments. Monocle analysis is based on scRNA-sequencing data in Fig. 1c, n = 8 biological replicates, 4 independent experiments.

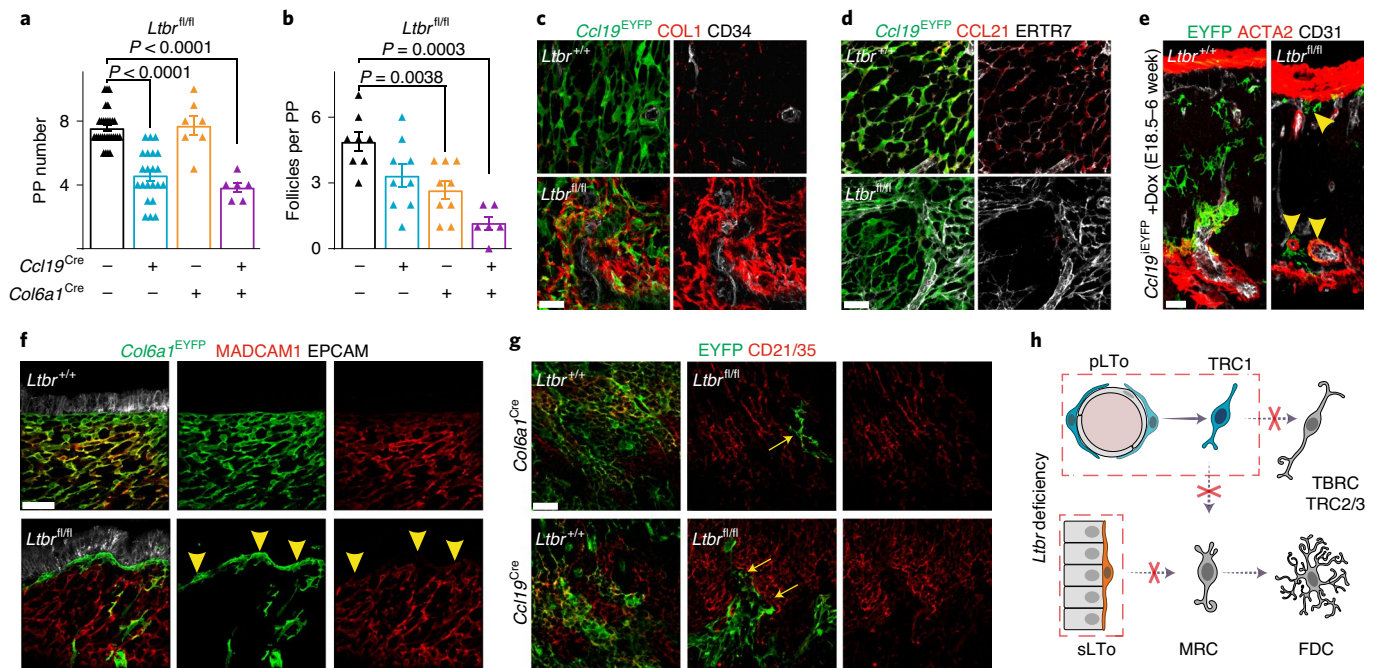


Fig. 3 | Lymphotoxin- β receptor signaling-dependent FRC organization in PP microdomains. **a, b, Number of PPs and B cell follicles in PPs from adult *Ltbr^{fl/fl}* ($n = 30$), *Ccl19^{Cre}Ltbr^{fl/fl}* ($n = 22$), *Col6a1^{Cre}Ltbr^{fl/fl}* ($n = 7$) and *Ccl19^{Cre}Col6a1^{Cre}Ltbr^{fl/fl}* ($n = 6$) mice. **c, d**, Confocal microscopy analysis showing EYFP⁺ FRC networks in adult PP. **e**, Images depict EYFP⁺ cells representing progeny of E18.5 progenitors in the T cell zone of adult PP of inducible *Ccl19^{EYFP}* mice. Arrowheads indicate perivascular location of *Ltbr*-deficient EYFP⁺ cells. **f**, Confocal microscopy of EYFP⁺ FRC networks in the SED. **g**, B cell follicle. Arrowheads in **f** indicate subepithelial YFP⁺ cells, arrows in **g** indicate EYFP⁺CD21/35⁻ cells. **h**, Schematic depiction of LT β R signaling in FRC differentiation. Scale bars, 20 μ m (**c–e, g**), 30 μ m (**f**). Images are representative of 3–4 mice per group, and at least two independent experiments. (**a, b**) The s.e.m. is indicated; P values as per two-tailed Mann–Whitney U -test.**

expression in *Ccl19^{EYFP+}* and *Col6a1^{EYFP+}* cells completely blocked FDC maturation (Extended Data Fig. 5f) lending further support to the interpretation that the two FRC lineages cooperate in the generation of productive niches for B cells in PPs. In sum, these data indicate that perivascular, *Ccl19*-expressing LTo cells differentiate into TRC2/3, TBRCs, some MRCs and FDCs in an LT β R-dependent fashion, while subepithelial, *Col6a1*-expressing subepithelial LTo cells depend on LT β R signals to generate MRCs and FDCs (Fig. 3h).

Tnfr1^{-/-} mice show reduced numbers of PPs with defective lymphoid segregation, and TNF signaling is necessary for FDC differentiation and GC formation^{30,31}. High-resolution confocal microscopic analysis of the two FRC lineages in *Tnfr1^{-/-}* PPs revealed an extensive *Ccl19^{GFP+}* network located between the muscular layer and the intestinal villi, characterized by the expression of the TRC markers CCL21 and ER-TR7 (Extended Data Fig. 6a). *Col6a1^{GFP+}* cells were located inside the intestinal villi, some of which were enlarged and contained GFP⁺RANKL⁺ MRC-like cells (Extended Data Fig. 6a). *Tnfr1* ablation in the *Ccl19^{Cre}* or *Col6a1^{Cre}* lineages did not significantly affect PP formation or B cell follicle maturation (Fig. 4a,b). However, when *Tnfr1* expression was deleted in both lineages, B cell follicle numbers were reduced (Fig. 4b) and B–T cell zone compartmentalization was impaired (Extended Data Fig. 6b), suggesting that both FRC lineages contribute to the TNF-mediated formation of proper B cell environments. To assess the impact of TNFR1 signaling on FRC differentiation in more detail, we characterized the topology and FRC marker expression in both *Ccl19^{Cre}* and *Col6a1^{Cre}* lineages. While TRC and MRC networks in *Ccl19^{GFP}Tnfr1^{fl/fl}* PPs (Fig. 4c and Extended Data Fig. 6c) were not affected by the lack of TNF stimulation, maturation of GFP⁺ FDCs was strongly reduced (Fig. 4d). Likewise, *Tnfr1* deletion in the *Col6a1* lineage blocked the differentiation of FDCs, while MRC development was affected

to a lesser extent (Fig. 4e–h and Extended Data Fig. 6d). Previous work has shown that FRCs in PPs regulate the FAE maturation and the differentiation of transcytosing microfold (M) cells by producing receptor activator of NF- κ B ligand (RANKL)^{32,33}. We found that *Tnfr1* deletion in the *Col6a1* lineage impaired the differentiation of M cells (Extended Data Fig. 6e) and induced the formation of proliferative crypts in the epithelial dome (Extended Data Fig. 6f), which correlated with a reduction in the expression of *Tnfsf11* and other molecules involved in M cell differentiation (Extended Data Fig. 6g). Although *Tnfr1* deletion in neither of the FRC lineages altered PP immune cell composition (Extended Data Fig. 6h), both the induction of GC B cells (Extended Data Fig. 6i) and the production of specific IgA upon oral immunization with cholera toxin were reduced in *Col6a1^{Cre}Tnfr1^{fl/fl}* PPs (Extended Data Fig. 6j), indicating specific lineage-restricted functions. Collectively, these data reveal that signaling via the LT β R is required for subset formation in both FRC lineages, while TNFR1 signaling enables lineage convergence through the formation of the MRC-to-FDC differentiation trajectory (Fig. 4i).

FRC lineage convergence governs intestinal homeostasis. To elaborate the functional importance of the TNFR1-dependent FRC lineage convergence and the impact of B cell follicle organization, we employed a mouse model carrying a conditional gain-of-function *Tnfr1* allele (*Tnfr1^{CNEO}* (ref. 14)) (Fig. 5a and Extended Data Fig. 7a). As expected, *Tnfr1^{CNEO/-}* mice resembled the *Tnfr1^{-/-}* mouse phenotype, including a reduction in the number and size of PPs, a disorganized structure and absence of FDCs and GC B cells (Extended Data Fig. 7b,c). TNFR1 reactivation solely in the *Ccl19^{Cre}* lineage (*Ccl19^{Tnfr1-ON}*) resulted in the gain of both the number of PPs and B cell follicles when compared to *Tnfr1^{CNEO/-}* mice (Fig. 5b,c and Extended Data Fig. 7b). *Ccl19^{Tnfr1-ON}* PPs contained fewer immune

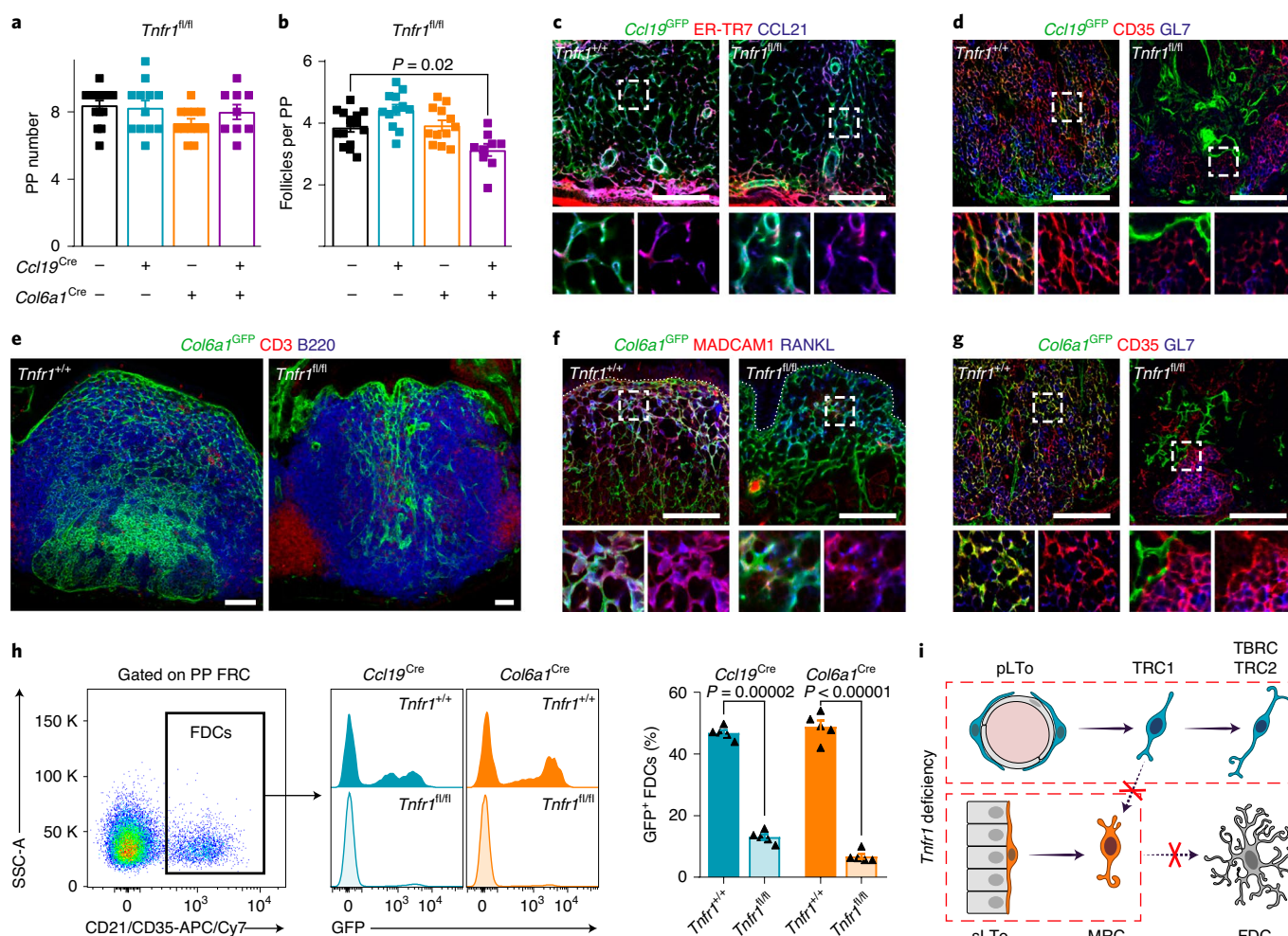


Fig. 4 | TNFR1 signaling in FRCs regulates follicle organization. **a,b**, Number of PPs (**a**) and B cell follicles in PPs (**b**) from adult *Tnfr1^{fl/fl}* ($n=15$), *Ccl19^{Cre}Tnfr1^{fl/fl}* ($n=12$), *Col6a1^{Cre}Tnfr1^{fl/fl}* ($n=12$) and *Ccl19^{Cre}Col6a1^{Cre}Tnfr1^{fl/fl}* ($n=9$) mice. **c,d**, Confocal microscopy pictures showing the targeting of CCL21⁺ER-TR7⁺ TRCs (**c**) and CD35⁺ FDCs (**d**) by *Ccl19^{Cre}* in a *Tnfr1^{+/+}* and *Tnfr1^{fl/fl}* background. **e-g**, Confocal microscopy showing the topology and phenotype of *Col6a1^{Cre}* FRC networks (CD3⁺B220⁺ (**e**); MADCAM1⁺RANKL⁺ (**f**); CD35⁺GL7⁺ (**g**)) in *Tnfr1^{+/+}* and *Tnfr1^{fl/fl}* PPs. **h**, Flow cytometry analysis showing the reduction of GFP⁺ FDCs after *Tnfr1* deletion in the *Col6a1^{Cre}* or *Ccl19^{Cre}* lineages. CD21/CD35⁺ FDCs are gated on the PP FRC population, as in Extended Data Fig. 1a ($n=5$ mice per genotype). **i**, Schematic depiction of TNFR1 signaling in FRC differentiation. Scale bars, 50 μ m. Boxes show magnified areas (**c,d,f,g**). Images are representative of 5–7 mice per group and at least two independent experiments. *P* values as one-way ANOVA (**a,b**) or two-tailed *t*-test (**h**). Mean and s.e.m. are indicated.

cells compared to *Tnfr1*-proficient PPs (Fig. 5d), indicating a compensatory role of the *Col6a1^{Cre}* lineage. Indeed, restoration of *Tnfr1* in the *Col6a1^{Cre}* lineage (*Col6a1^{Tnfr1-ON}*) fully recovered B cell follicle development and immune cell content (Fig. 5c,d), but not the number of PPs (Fig. 5b). Notably, TNFR1 reactivation in both lineages (*Ccl19/Col6a1^{Tnfr1-ON}*) led to the restoration of the number of PPs, B cell follicles and immune cells (Fig. 5b–d), confirming that TNFR1 signaling is required in both lineages for proper PP development.

Further analyses demonstrated that the structural segregation of B cell follicles and interfollicular T cell zones, as well as the formation of FDC-containing GCs, was restored with *Tnfr1* being re-expressed on either of the FRC lineages (Fig. 5e). Interestingly, cells of the *Ccl19^{Cre}* lineage showed a higher abundance and populated the whole PP except for the subepithelial region when *Tnfr1* expression was re-introduced (Fig. 5e, arrows). In contrast, re-expression of *Tnfr1* in the *Col6a1^{Cre}* lineage restored MRC networks in the subepithelial dome extending to the FDC network in the B cell follicle (Fig. 5e, arrowheads), further supporting the

notion that the MRC-to-FDC transition is mainly dependent on TNFR1 signaling.

Similar to the above observations using *Tnfr1* conditional knockout mice, we found that restoration of TNFR1 signaling in the *Col6a1^{Cre}* lineage was sufficient to promote the normal differentiation of M cells in the follicle-associated epithelium (Fig. 5f,g). Restoration of *Tnfr1* expression in the *Col6a1^{Cre}* lineage led to recovery of *Tnfsf11* and *Cxcl13* expression, whereas the expression of T cell zone chemokine *Ccl19* and *Ccl21* required TNFR1 signaling in the *Ccl19^{Cre}* lineage (Extended Data Fig. 7d). Both *Ccl19^{Tnfr1-ON}* and *Col6a1^{Tnfr1-ON}* PPs re-established GC B cell activation and the production of specific IgA upon oral immunization with cholera toxin, when compared to *Tnfr1^{CNEO/-}* PPs (Fig. 5h,i). Aside from mediating enteric pathogen and toxin neutralization, IgA is responsible for establishing symbiotic relations between the host and intestinal microbiota³⁴. To assess to what extent FRC-dependent PP integrity affects intestinal IgA responses, we performed 16S ribosomal RNA sequencing of IgA-bound bacteria. Fecal samples

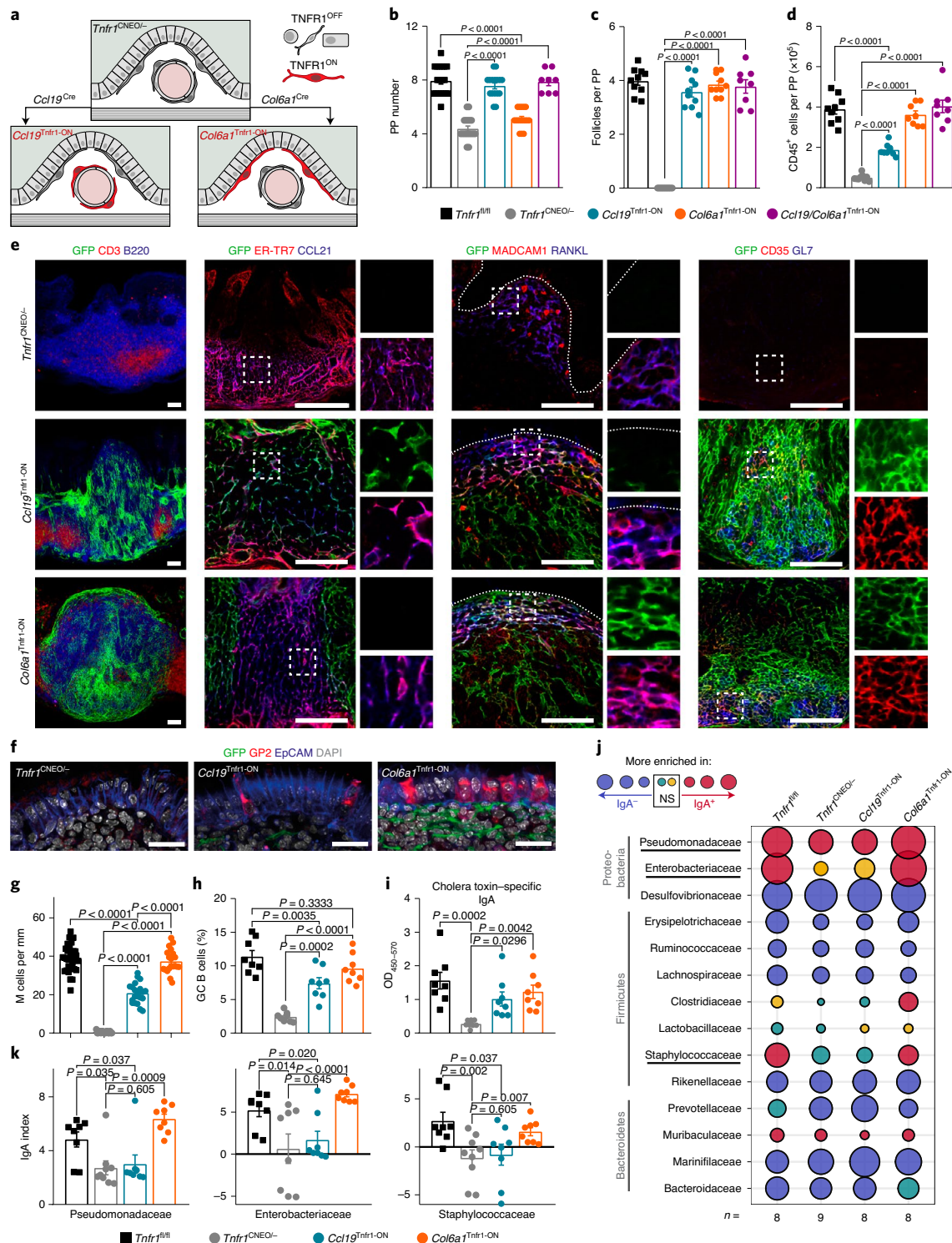


Fig. 5 | *Tnfr1* expression by either of the two mesenchymal populations is sufficient to organize PPs. **a**, Schematic of *Tnfr1*^{CNEO} model. **b-d**, Quantification of the number of PPs (**b**), follicles per PP (**c**) and CD45⁺ (**d**) cells in adult *Tnfr1*^{fl/fl}, *Tnfr1*^{CNEO/-}, *Ccl19*^{Tnfr1-ON}, *Col6a1*^{Tnfr1-ON} and *Ccl19/Col6a1*^{Tnfr1-ON} mice.

e, Histological analysis of adult PPs from *Tnfr1*^{CNEO/-}, *Tnfr1*^{Ccl19-ON} and *Tnfr1*^{Col6a1-ON} mice showing Cre-mediated GFP expression (green) and the indicated markers for B cells (B220), T cells (CD3), TRCs (ER-TR7 and CCL21), MRCs (MADCAM1 and RANKL), FDCs (CD35) and germinal center B cells (GL7). Boxes show magnified areas. Dotted lines mark the epithelial layer. Scale bar, 50 μm. Representative of five mice per group. **f,g**, Confocal images (**f**) and quantification (**g**) of GP2⁺ M cells in the epithelial dome. Scale bar, 25 μm. Several PP follicles from *Tnfr1*^{fl/fl} (*n* = 6), *Tnfr1*^{CNEO/-} (*n* = 4), *Ccl19*^{Tnfr1-ON} (*n* = 5) and *Col6a1*^{Tnfr1-ON} (*n* = 5) mice were analyzed. **h**, Flow cytometric analyses characterizing the proportion of GC B cells in PPs (*n* = 8 mice per genotype).

i, ELISA of cholera toxin-specific IgA response. Mice were orally immunized with cholera toxin 1 week before the examination (*n* = 8 mice per genotype).

OD, optical density. **j**, Bubble plot showing IgA responses to major bacteria taxa, defined by the IgA index. Threshold for significant enrichment was determined by paired Wilcoxon test (*P* < 0.05; NS, not significant).

k, IgA index in fecal bacterial samples of Pseudomonadaceae, Enterobacteriaceae and Staphylococcaceae from the indicated genotypes (*Tnfr1*^{fl/fl} *n* = 8, *Tnfr1*^{CNEO/-} *n* = 9, *Ccl19*^{Tnfr1-ON} *n* = 8, *Col6a1*^{Tnfr1-ON} *n* = 8). *P* values as one-way ANOVA (**b-d,g-i,k**) or Wilcoxon rank sum test (**j**). Mean and s.e.m. are indicated.

from *Tnfr1*^{CNEO/-} mice showed no overt changes in bacterial families enriched in the IgA⁻ fraction compared to samples from *Tnfr1*-proficient mice (Fig. 5j). However, a significant reduction in IgA production against three highly coated bacterial families (Pseudomonadaceae, Enterobacteriaceae, Staphylococcaceae) was observed in *Tnfr1*-deficient mice (Fig. 5k and Supplementary Table 1). TNFR1 reactivation in *Col6a1*^{Tnfr1-ON}, but not in *Ccl19*^{Tnfr1-ON} PP, restored the IgA response and microbiota composition (Fig. 5k and Extended Data Fig. 6e–j). Collectively, TNFR1-dependent FRC lineage convergence orchestrates PP organogenesis and functionality with a particular need for TNF-mediated FDC maturation in the *Col6a1*^{Cre} lineage, to optimize IgA output against commensal bacteria.

FRC lineage convergence supports anticoronavirus B cell responses. FRCs of lymph nodes have been recognized as key players for the generation of protective immunity against viral infections^{10,11,27}. PP FRCs of the *Ccl19*^{Cre} lineage regulate intestinal inflammation during infection with the murine coronavirus (M-CoV) via IL-15-mediated control of group 1 ILCs⁷. High expression of the nucleoprotein (NP) of M-CoV could already be detected in the SED and T cell zones of PPs 36 h after oral infection (Fig. 6a,b). We found elevated *Ccl19*^{Cre} activity in FDC and MRC networks at day 7 post infection (Fig. 6c). Subepithelial FRC networks exhibited only minor *Ccl19*^{Cre} activity (Fig. 6d), indicating that FRC lineage identity was largely preserved during intestinal M-CoV infection. Since convergence of FRC lineages in the MRC–FDC differentiation trajectory was strictly dependent on *Tnfr1* expression, we assessed M-CoV infection in *Tnfr1*^{CNEO/-} and in lineage-specific *Tnfr1* gain-of-function mice. Restriction of *Tnfr1* expression to the *Ccl19*^{Cre} lineage (*Ccl19*^{Tnfr1-ON}), but not to the *Col6a1*^{Cre} lineage (*Col6a1*^{Tnfr1-ON}), was sufficient for the generation of IgA⁺ plasmablasts (Fig. 6e,f), and the restoration of M-CoV-specific IgA⁺ antibody-secreting cells (Fig. 6g) in the lamina propria of infected mice to normal levels. These data indicate that TNFR1-dependent activation of the *Ccl19*-Cre lineage not only restores PP organogenesis, but also critically contributes to anticoronavirus IgA responses against M-CoV infection.

Discussion

We have provided an extensive molecular characterization of the PP FRC landscape and the mechanisms that govern PP development and patterning. Consecutive activation of perivascular and subepithelial fibroblast lineages underpins the mosaic nature of PP FRCs. The convergence of both FRC lineages towards the MRC–FDC subsets ensures robust establishment of microenvironmental niches that secure B cell activation and differentiation. Synergistic and partially compensatory mechanisms between both lineages grant the induction of adaptive immune responses against intestinal viral infection and the IgA-dependent regulation of commensal microbiota.

Our study reveals unique patterning in the FRC landscape in PPs when compared to other secondary lymphoid organs. FRCs in the splenic white pulp and lymph node originate solely from perivascular LTo cells, with splenic FRC progenitors being located around central arterioles of the primordial white pulp¹², while FRC progenitors in lymph nodes appear to reside around venules of the anlagen^{13,20}. We found that LT_i cell accumulation in PP anlagen occurs first in a mesh of postcapillary venules in proximity to the muscular layer, leading to LT β R-dependent FRC maturation from perivascular LTo cells. In an important step following the initial activation of perivascular LTo cells, and concomitant with increased immigration of T and B cells, progressive LT β R-dependent activation of the subepithelial LTo cells precipitates the formation of MRC networks. Importantly, TNF-mediated stimulation of progenitor cells from both the *Ccl19*^{Cre} and the *Col6a1*^{Cre} lineages resulted in the activation of the MRC–FDC differentiation trajectory. Since microbial

colonization determines FDC formation in intestinal lymphoid organs³⁵ and TLR4-mediated stimulation further promotes FDC activation³⁶, it is most likely that pre- and postweaning exposure to microbial components drives the TNF-mediated MRC and FDC maturation in the two FRC lineages. In addition, other stromal cell populations in secondary lymphoid organs, such as blood and lymphatic endothelial cells in lymph nodes^{37,38}, express the TNFR1 and can therefore contribute to the global activation of the stromal cell infrastructure. Hence, FRC lineage convergence in PPs probably underpins—in concert with other activated stromal cells—the recently described weaning reaction that grants maturation of the immune system³⁹ and is important to prevent diseases such as allergies, or colitis later in life.

Recent single-cell transcriptomics analyses have begun to unravel the complexity of FRC niches in secondary lymphoid organs. It appears that lymph nodes harbor seven to nine different FRC subsets^{10,11}, while the splenic white pulp is formed by four main FRC populations¹². Our study reveals the presence of six major PP FRC subsets, which relate to the previously described subsets in lymph nodes and spleen. MRCs appear to underpin the antigen sampling zone being present in the marginal zone of the splenic white pulp, the subcapsular sinus in lymph nodes and the subepithelial dome of PPs. The PP data confirm that *Madcam1*, together with the high expression of *Cxcl13*, appears to be the best suitable cross-organ MRC marker, also on the protein level^{10,11}. Interestingly, PP MRCs show the expression of FDC genes, such as *Coch*, *Sncg*, *Sox9* (ref. 11), suggesting that the PP microenvironment requires particular functional adaptations of MRCs. PP FDCs share the high expression of complement receptors (CD25/35) with their counterparts in other lymphoid organs^{10–12}, but show uniquely high expression of the high affinity receptor for IgM and IgA. Here, we did not find further PP FDC segregation into light and dark zone subsets, a hallmark of activated B cell zones with an ongoing GC reaction in lymph nodes^{11,40}. Likewise, TBRC in PPs with the *Acta2*^{hi}*Madcam1*^{hi} phenotype appear to exhibit different functional properties when compared to *Ccl19/Ccl21*^{lo} *Madcam1*⁻ reticular cells at the lymph node T–B cell zone border¹⁰. The FRC population labeled as TRC1 in PPs is located around blood vessels and shares properties with perivascular stromal cells of lymph nodes, such as the stemness marker *Cd34* (ref. 10) and the splenic perivascular reticular cell markers *Ly6a* (stem cell antigen-1), *Acta2* and *Pdgfrb*¹². We consider it highly likely that the perivascular TRC1 population harbors multipotent FRC progenitors in the adult PPs to replenish TRC2 and 3 in the T cell zone, TBRCs and probably B cell zone FRC populations. Two TRC subsets (TRC2 and 3) appeared in our analysis, with TRC2 exhibiting high expression of interferon-induced genes. Such activated FRC subsets appear to be situated specifically in regions such as SEDs and T cell zones where exposure to antigen is high and where early infection with M-CoV was detected. Infection with the human severe acute respiratory syndrome coronavirus 2 (SARS-CoV-2) not only induces immunopathological processes in the respiratory system, but is also accompanied by gastrointestinal complications⁴¹. Protection against intestinal pathogens and the maintenance of a protective barrier against commensal bacteria is maintained to a large extent by IgA-producing B cells that are induced in Peyer's patches^{42–44}. Thus, it is conceivable that SARS-CoV-2 infection-associated gastrointestinal disease could be underpinned by deficiencies in antiviral processes in PPs, including the insufficient generation of immune cell niches by dysfunctional FRC networks.

FRC differentiation from the different progenitor populations in PPs is a structured and hierarchical process. Signaling via the LT β R appears to be the main switch, a 'signal 1' as suggested for splenic FRCs¹² that determines whether perivascular or subepithelial fibroblastic progenitors enter the differentiation trajectory towards immune-interacting fibroblasts. TNF-dependent differentiation

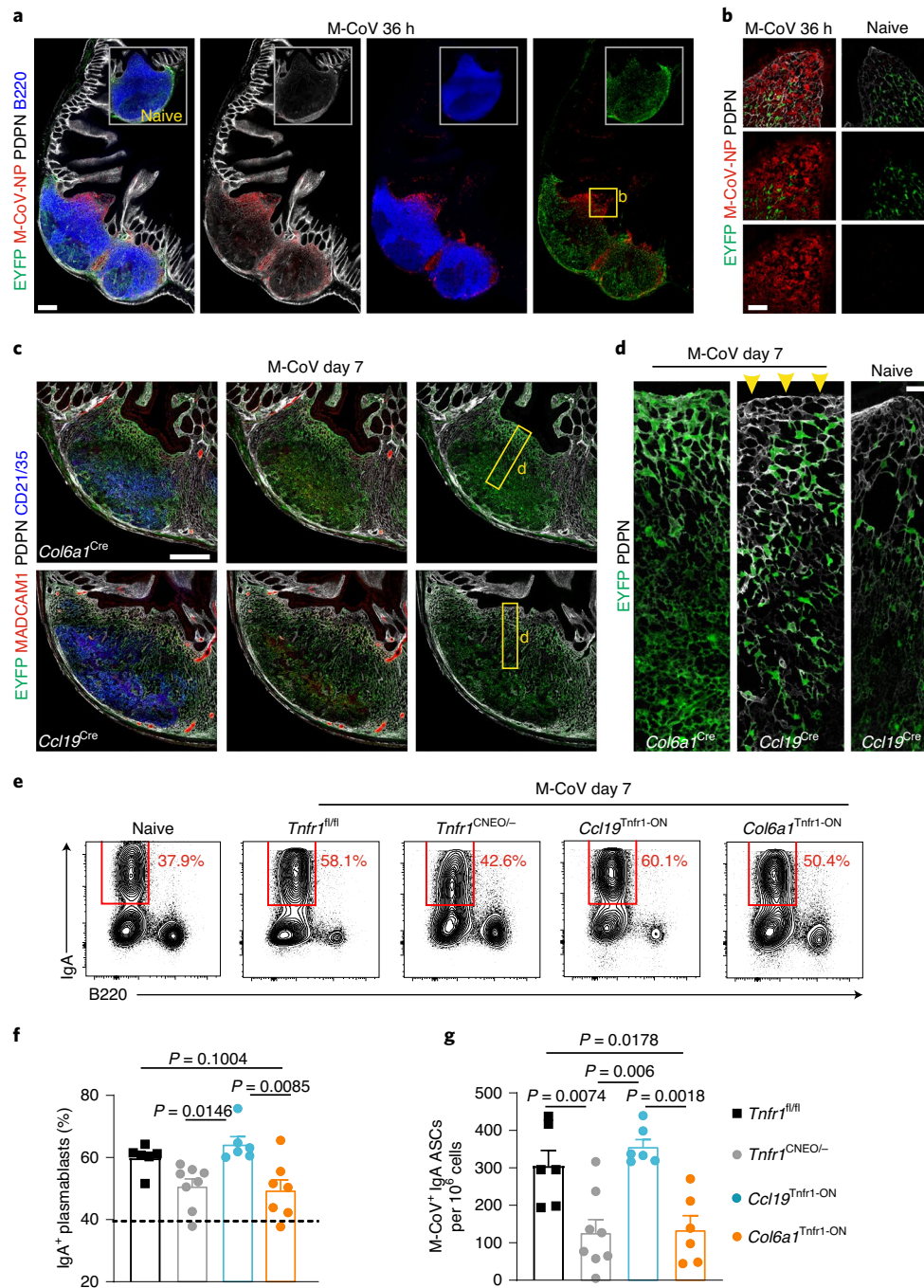


Fig. 6 | FRC lineage convergence and intestinal coronavirus infection. **a, b**, Confocal microscopy analysis of Peyer's patches collected from *Ccl19*^{EYFP} mice, which were intraorally infected with M-CoV 36 h before analysis. Inset images show B cell follicles from noninfected (naive) littermate control mice (**a**). Boxes indicate representative regions of the SED (**b**). **c, d**, Images depict B cell follicles, SEDs and perifollicular T cell zones of PPs from M-CoV-infected mice at day 7 after infection (**c**). Boxes indicate representative regions shown in **d**. Arrowheads in **d** indicate lack of EYFP expression under the follicle-associated epithelium. **e, f**, Flow cytometric analysis of IgA-producing plasmablasts (**f**) and B cells (**e**) in the lamina propria of M-CoV-infected mice (*Tnfr1*^{fl/fl} *n* = 6, *Tnfr1*^{CNEO-/-} *n* = 8, *Ccl19*^{Tnfr1-ON} *n* = 6, *Col6a1*^{Tnfr1-ON} *n* = 6) at day 7 after infection. Numbers indicate the percentage of cells in the gated population. **g**, Enumeration of M-CoV⁺ IgA-secreting cells (ASCs) per million B cells. Scale bars, 200 μ m (**a, c**), 30 μ m (**b**), 10 μ m (**d**). Images are representative of 3–4 mice per group and at least two independent experiments. Mean percentages and s.e.m. are indicated; *P* values as one-way ANOVA (**f, g**).

of FDCs represents a mandatory second signal and highlights the potential of the two different PP FRC lineages to converge in the FDC subset. However, TNF-mediated stimulation can override the requirement of LT β R-dependent FRC activation, as exemplified in nonclassical secondary lymphoid organs, such as a fat-associated lymphoid clusters (for example, omental milky spots), which develop

and function under conditions of *Ltbr*-deficiency⁴⁵. Clearly, FRC convergence from different fibroblastic progenitor populations and the utilization of complementary mechanisms provides a fail-safe mechanism for the generation of immune-stimulating environments, not only in secondary lymphoid organs, but also in differentiated inflammatory lesions that are commonly known as tertiary

lymphoid structures⁴⁶. In the future, it will be interesting to investigate whether the existence of different fibroblast sources and the mechanisms that we have uncovered here can also contribute to development of other tissues and participate in pathologies, such as chronic inflammation, fibrosis or tumorigenesis.

Online content

Any methods, additional references, Nature Research reporting summaries, source data, extended data, supplementary information, acknowledgements, peer review information; details of author contributions and competing interests; and statements of data and code availability are available at <https://doi.org/10.1038/s41590-021-00894-5>.

Received: 11 May 2020; Accepted: 3 February 2021;

Published online: 11 March 2021

References

- Caruso, R., Lo, B. C. & Núñez, G. Host-microbiota interactions in inflammatory bowel disease. *Nat. Rev. Immunol.* **20**, 411–426 (2020).
- Lasry, A., Zinger, A. & Ben-Neriah, Y. Inflammatory networks underlying colorectal cancer. *Nat. Immunol.* **17**, 230–240 (2016).
- Neurath, M. F. Targeting immune cell circuits and trafficking in inflammatory bowel disease. *Nat. Immunol.* **20**, 970–979 (2019).
- Macpherson, A. J., Geuking, M. B., Slack, E., Hapfelmeier, S. & McCoy, K. D. The habitat, double life, citizenship, and forgetfulness of IgA. *Immunol. Rev.* **245**, 132–146 (2012).
- Macpherson, A. J. & Uhr, T. Induction of protective IgA by intestinal dendritic cells carrying commensal bacteria. *Science* **303**, 1662–1665 (2004).
- Chang, J. E., Buechler, M. B., Gressier, E., Turley, S. J. & Carroll, M. C. Mechanosensing by Peyer's patch stroma regulates lymphocyte migration and mucosal antibody responses. *Nat. Immunol.* **20**, 1506–1516 (2019).
- Gil-Cruz, C. et al. Fibroblastic reticular cells regulate intestinal inflammation via IL-15-mediated control of group 1 ILCs. *Nat. Immunol.* **17**, 1388–1396 (2016).
- Link, A. et al. Fibroblastic reticular cells in lymph nodes regulate the homeostasis of naive T cells. *Nat. Immunol.* **8**, 1255–1265 (2007).
- Chai, Q. et al. Maturation of lymph node fibroblastic reticular cells from myofibroblastic precursors is critical for antiviral immunity. *Immunity* **38**, 1013–1024 (2013).
- Rodda, L. B. et al. Single-cell RNA sequencing of lymph node stromal cells reveals niche-associated heterogeneity. *Immunity* **48**, 1014–1028.e6 (2018).
- Pikor, N. B. et al. Remodeling of light and dark zone follicular dendritic cells governs germinal center responses. *Nat. Immunol.* **21**, 649–659 (2020).
- Cheng, H. W. et al. Origin and differentiation trajectories of fibroblastic reticular cells in the splenic white pulp. *Nat. Commun.* **10**, 1739 (2019).
- Denton, A. E., Carr, E. J., Magiera, L. P., Watts, A. J. B. & Fearon, D. T. Embryonic FAP⁺ lymphoid tissue organizer cells generate the reticular network of adult lymph nodes. *J. Exp. Med.* **216**, 2242–2252 (2019).
- Jarjour, M. et al. Fate mapping reveals origin and dynamics of lymph node follicular dendritic cells. *J. Exp. Med.* **211**, 1109–1122 (2014).
- Krishnamurthy, A. T. & Turley, S. J. Lymph node stromal cells: cartographers of the immune system. *Nat. Immunol.* **21**, 369–380 (2020).
- Onder, L. & Ludewig, B. A fresh view on lymph node organogenesis. *Trends Immunol.* **39**, 775–787 (2018).
- Jeucken, K. C. M., Koning, J. J., Mebius, R. E. & Tas, S. W. The role of endothelial cells and TNF-receptor superfamily members in lymphoid organogenesis and function during health and inflammation. *Front. Immunol.* **10**, 2700 (2019).
- Veiga-Fernandes, H. et al. Tyrosine kinase receptor RET is a key regulator of Peyer's patch organogenesis. *Nature* **446**, 547–551 (2007).
- Yoshida, H. et al. IL-7 receptor α^+ CD3⁻ cells in the embryonic intestine induces the organizing center of Peyer's patches. *Int. Immunol.* **11**, 643–655 (1999).
- Onder, L. et al. Lymphatic endothelial cells control initiation of lymph node organogenesis. *Immunity* **47**, 80–92 (2017).
- Nakagawa, R., Togawa, A., Nagasawa, T. & Nishikawa, S. Peyer's patch inducer cells play a leading role in the formation of B and T cell zone architecture. *J. Immunol.* **190**, 3309–3318 (2013).
- Debard, N., Sierro, F., Browning, J. & Kraehenbuhl, J. P. Effect of mature lymphocytes and lymphotoxin on the development of the follicle-associated epithelium and M cells in mouse Peyer's patches. *Gastroenterology* **120**, 1173–1182 (2001).
- Victoratos, P. et al. FDC-specific functions of p55TNFR and IKK2 in the development of FDC networks and of antibody responses. *Immunity* **24**, 65–77 (2006).
- Prados, A., Kollias, G. & Koliarakis, V. CollagenVI-Cre mice: a new tool to target stromal cells in secondary lymphoid organs. *Sci. Rep.* **6**, 33027 (2016).
- Kinchen, J. et al. Structural remodeling of the human colonic mesenchyme in inflammatory bowel disease. *Cell* **175**, 372–386.e17 (2018).
- Afanasyeva, M. A. et al. Clusterin is a potential lymphotoxin beta receptor target that is upregulated and accumulates in germinal centers of mouse spleen during immune response. *PLoS ONE* **9**, e98349 (2014).
- Perez-Shibayama, C. et al. Type I interferon signaling in fibroblastic reticular cells prevents exhaustive activation of antiviral CD8⁺ T cells. *Sci. Immunol.* **5**, eabb7066 (2020).
- Qiu, X. et al. Reversed graph embedding resolves complex single-cell trajectories. *Nat. Methods* **14**, 979–982 (2017).
- Livet, J. et al. Transgenic strategies for combinatorial expression of fluorescent proteins in the nervous system. *Nature* **450**, 56–62 (2007).
- Pasparakis, M. et al. Peyer's patch organogenesis is intact yet formation of B lymphocyte follicles is defective in peripheral lymphoid organs of mice deficient for tumor necrosis factor and its 55-kDa receptor. *Proc. Natl Acad. Sci. USA* **94**, 6319–6323 (1997).
- Neumann, B., Luz, A., Pfeffer, K. & Holzmann, B. Defective Peyer's patch organogenesis in mice lacking the 55-kD receptor for tumor necrosis factor. *J. Exp. Med.* **184**, 259–264 (1996).
- Nagashima, K. et al. Identification of subepithelial mesenchymal cells that induce IgA and diversify gut microbiota. *Nat. Immunol.* **18**, 675–682 (2017).
- Nagashima, K. et al. Targeted deletion of RANKL in M cell inducer cells by the Col6a1-Cre driver. *Biochem. Biophys. Res. Commun.* **493**, 437–443 (2017).
- Macpherson, A. J., Yilmaz, B., Limentakis, J. P. & Ganai-Vonarburg, S. C. IgA function in relation to the intestinal microbiota. *Annu. Rev. Immunol.* **36**, 359–381 (2018).
- Hanson, N. B. & Lanning, D. K. Microbial induction of B and T cell areas in rabbit appendix. *Dev. Comp. Immunol.* **32**, 980–991 (2008).
- El Shikh, M. E., El Sayed, R. M., Wu, Y., Szakal, A. K. & Tew, J. G. TLR4 on follicular dendritic cells: an activation pathway that promotes accessory activity. *J. Immunol.* **179**, 4444–4450 (2007).
- Fujimoto, N. et al. Single-cell mapping reveals new markers and functions of lymphatic endothelial cells in lymph nodes. *PLoS Biol.* **18**, e3000704 (2020).
- Brulois, K. et al. A molecular map of murine lymph node blood vascular endothelium at single cell resolution. *Nat. Commun.* **11**, 3798 (2020).
- Al Nabhani, Z. et al. A weaning reaction to microbiota is required for resistance to immunopathologies in the adult. *Immunity* **50**, 1276–1288.e5 (2019).
- Rodda, L. B., Bannard, O., Ludewig, B., Nagasawa, T. & Cyster, J. G. Phenotypic and morphological properties of germinal center dark zone Cxcl12-expressing reticular cells. *J. Immunol.* **195**, 4781–4791 (2015).
- Lamers, M. M. et al. SARS-CoV-2 productively infects human gut enterocytes. *Science* **369**, 50–54 (2020).
- Reboldi, A. & Cyster, J. G. Peyer's patches: organizing B-cell responses at the intestinal frontier. *Immunol. Rev.* **271**, 230–245 (2016).
- Craig, S. W. & Cebra, J. J. Peyer's patches: an enriched source of precursors for IgA-producing immunocytes in the rabbit. *J. Exp. Med.* **134**, 188–200 (1971).
- Ansaldi, E. et al. *Akkermansia muciniphila* induces intestinal adaptive immune responses during homeostasis. *Science* **364**, 1179–1184 (2019).
- Benezech, C. et al. Inflammation-induced formation of fat-associated lymphoid clusters. *Nat. Immunol.* **16**, 819–828 (2015).
- Buckley, C. D., Barone, F., Nayar, S., Benezech, C. & Caamano, J. Stromal cells in chronic inflammation and tertiary lymphoid organ formation. *Annu. Rev. Immunol.* **33**, 715–745 (2015).

Publisher's note Springer Nature remains neutral with regard to jurisdictional claims in published maps and institutional affiliations.

© The Author(s), under exclusive licence to Springer Nature America, Inc. 2021

Methods

Mice. *R26^{EYFP}*, *R26^{nlT/mG}* and *R26^{Brainbow2.1}* reporter mice and *Rag1^{-/-}* mice were obtained from the Jackson Laboratory. The *Ccl19^{Cre}* (ref. ⁹), *Col6a1^{Cre}* (ref. ⁴⁷), *Ccl19^{Tia}* (ref. ¹²), *Lib1^{fl/fl}* (ref. ⁴⁸), *Tnfr1^{-/-}* (ref. ⁴⁹), *Tnfr1^{fl/fl}* (ref. ⁵⁰), *Tnfr1^{CNEO}* (ref. ²³) strains were described previously. Fate-mapping experiments were performed via treating the pregnant dams with 1 mg doxycycline (Sigma-Aldrich) intraperitoneally and maintenance of doxycycline in the drinking water (1 mg ml⁻¹). For the commensal microbiota studies, mice were housed in a single room and soiled cage bedding was routinely mixed twice per week and distributed among all cages from weaning (4 weeks old) until the onset of the study (10–12 weeks old). All mice were bred and maintained on a C57BL/6 genetic background in the animal facilities of the Biomedical Sciences Research Center “Alexander Fleming” and the Kantonsspital St. Gallen under specific pathogen-free conditions.

Experiments were performed in accordance with all current European and national legislation and were approved by the Institutional Committee of Protocol Evaluation in conjunction with the Veterinary Service Management of the Hellenic Republic Prefecture of Attika and the Swiss federal and cantonal guidelines (Tierschutzgesetz) under the permissions SG01/18, SG12/17, SG11/19 and SG08/18 granted by the Veterinary Office of the Kanton of St. Gallen.

Droplet-based single-cell RNA-sequencing analysis. Complementary DNA libraries were generated on a 10x Chromium (10x Genomics)⁵¹ following the recommended protocol for the Chromium Single Cell 3' Reagent Kit (v2 Chemistry and v3 Chemistry) and libraries were sequenced on a NovaSeq 6000 sequencing system from Illumina at the Functional Genomic Center, Zurich. Cell Ranger (v3.0.1)⁵² was used for an initial preprocessing of sequencing files, including mapping to Ensembl GRCh38.94 release as reference. Subsequent quality control was run in R v3.6.0 utilizing functions from scater R/Bioconductor package (v.1.11.2)⁵³ and included removal of damaged, cycling and contaminating cells on the basis of several criteria: (1) very high or low unique molecular identifier (UMI) counts (>2.5 median absolute deviation from the median across all cells); (2) very high or low total number of detected genes (>2.5 median absolute deviation from the median across all cells); (3) high mitochondrial gene content (>2.5 median absolute deviations above the median across all cells); (4) expression of one of the cell cycle markers *Top2a*, *Mki67*, *Cenpf* or *Pclaf*; (5) expression of any of the contamination markers *Lyve1*, *Cldn5*, *Ptprc*, *Cd79a*, *Vill*, *Fcer1g*, *Gfap*, *S100b*, *Cd79b* or high expression of *Cdh5*.

A total of 7,727 cells and 26,056 genes expressed in more than one cell remained after quality control, with 3,374 cells expressing *Eyfp*. First, canonical correlation analysis as implemented in the Seurat package (v.3.1.1)⁵⁴ running in R v3.6.2 was used to integrate data across batches (the first 17 correlation components were included for integration). Next, all cells remaining after quality control were analyzed together, and finally only EYFP-expressing cells were re-analyzed. Downstream analysis included normalization, scaling, dimensional reduction with principal component analysis (PCA) and UMAP and graph-based clustering utilizing functions from the Seurat package. Clusters were characterized on the basis of the expression of canonical marker genes as well as unbiased cluster markers inferred from the Wilcoxon test, as implemented in the FindMarkers function of the Seurat package.

Trajectory analysis. Differentiation trajectories for FRC clusters were reconstructed using the Monocle 3 analysis toolkit (v.0.2.0) running in R v3.6.2. Briefly, cells were assigned to partitions on the basis of the calculated UMAP reduction and trajectories were inferred running the `learn_graph` function as implemented in the `monocle3` package with parameters `minimal_branch_length = 30`, `L1.gamma = 0.1` and `L1.sigma = 0.05` to smooth graphs.

Antibodies. Anti-CD3 (17A2, AF594, 100240), anti-CD21/CD35 (7E9, APC-Cy7, 123418), anti-CD31 (390, PerCP-Cy5.5, 102420), anti-CD45 (30-F11, AF700, 103128), anti-B220 (RA3-6B2, biotin, 103204), anti-IgD (11-26c.2a, APC-Cy7, 405716), anti-MADCAM-1 (MECA-367, purified, 120702; MECA-367, biotin, 120706) and anti-VCAM-1 (429, PE-Cy7, 105720) were purchased from BioLegend. Anti- α SMA (1A4, eFluor660, 50-9760-82), anti-CD3e (145-2C11, PE-Cy7, 25-0031-82), anti-CD4 (RM4-5, AF700, 56-0042-82), anti-EpCAM (G8.8, purified, 14-5791-81), anti-GL7 (GL7, biotin, 13-5902-82), anti-IgA (mA-6E1, PE, 12-4204-82), anti-podoplanin (eBio8.1.1, eFluor660, 50-5381-82), anti-M-CoV-NP (J3.3), anti-CD34 (RAM34, biotin, 13-0341-82) and anti-RANKL (IK22/5, biotin, 13-5952-82) were purchased from ThermoFisher. Anti-CD31 (MEC13.3, purified, 550274), anti-CD35 (8C12, purified, 558768), anti-B220 (RA3-6B2, PE-CF594, 562290) were purchased from BD Pharmingen. Anti-CCL21 (biotin, BAF457) was purchased from R&D Systems; anti-GP2 (2F11-C3, biotin, D278-6) was purchased from MBL; anti-collagen IV (purified, ab6586) and anti-ER-TR7 (purified, ab51824) were purchased from Abcam. Anti-YFP (purified, 632459) and anti-TOMATO (purified, 632496) were purchased from Takara. Anti-M-CoV-NP (J3.3, purified, kindly provided by S. Siddell, University of Würzburg). Unconjugated antibodies were detected with the following secondary antibodies: Alexa Fluor 594-conjugated goat anti-rat IgG (A11007), Alexa Fluor 594-conjugated goat anti-rabbit IgG (A-11012), Alexa Fluor 647-conjugated goat anti-rat IgG (A21247), all purchased from ThermoFisher. Biotinylated

antibodies were detected using AF647-Streptavidin (S21374) from ThermoFisher and PE-Cy5- (554062) or APC-Streptavidin (554067) from BD Pharmingen. RANKL and CCL21 expression were detected using the Tyramide SuperBoost Kit (ThermoFisher, B40936).

Cell isolation and flow cytometry. PPs were collected and washed with cold PBS. Epithelial cells were removed after incubation in HBSS supplemented with 5 mM EDTA, 1 mM DTT and 20 μ M HEPES at pH 7.2 for 15 min at 37 °C. The remaining tissue was digested using an enzyme mix consisting of HBSS containing 10% fetal bovine serum, 0.8 mg ml⁻¹ dispase, 0.1 mg ml⁻¹ collagenase P (Roche) and 0.1 mg ml⁻¹ DNase I (Sigma) for 45 min at 37 °C, as described previously⁵⁵. Cells were washed with cold PBS and suspended in fluorescence-activated cell sorting (FACS) buffer (PBS supplemented with 0.5% BSA and 5 mM EDTA in PBS) at 10⁷ cells per ml. A cell suspension of 100 μ l suspension was blocked using 4% of normal mouse serum and was then incubated for 30 min at 4 °C with the indicated antibodies.

The isolation of cells from small intestine lamina propria was performed as previously described⁵⁶. Small intestines were flushed and after removal of Peyer patches, tissue was collected and incubated three times for 15 min at 20 °C under constant agitation with BSS containing 5% FCS (Lonza), 5 mM EDTA (Sigma), 10 mM HEPES (Sigma) at pH 7.2 and 1 mM DTT to dissociate the epithelial layer. The tissue was subsequently washed with BSS containing 10 mM HEPES at pH 7.2 and digested three times for 20 min at 37 °C with 120 μ g ml⁻¹ collagenase P (Roche), 25 μ g ml⁻¹ DNase I (Applichem) and 5 μ g ml⁻¹ dispase I (Roche) in RPMI 1640. After obtaining a single-cell suspension, cells were purified by a 30%–70% Percoll gradient. Single-cell suspensions were first stained with the fixable viability dye Zombie Aqua (BioLegend) and incubated for 30 min on ice; after washing, cells were incubated for 20 min at 4 °C in PBS containing 2% FCS and 10 mM EDTA with fluorochrome-labeled antibodies.

Finally, cells were sorted on a Bio-Rad S3 (Bio-Rad) or BD Melody cellsorter, acquired on a BD Canto II (both BD Bioscience) or LSR Fortessa and data were analyzed using Flowjo software (Tree Star).

Tissue processing and microscopy. Small intestines containing PPs were collected from adult mice, washed with PBS, fixed in 4% PFA for 1 h or overnight and immersed in 2% agarose. Section of 40–70 μ m were obtained using a Leica VT1200S vibratome and blocked in PBS containing 1% albumin and 0.1% saponin for 30 min. Embryo or newborn small intestine were washed, fixed in PFA 4% for 1 h and snap-frozen in an OCT-filled mold on a liquid nitrogen-cooled metal surface. Cryosections of 10 μ m thickness were rehydrated in wash buffer (0.1% saponin in PBS) for 5 min and blocked in PBS containing 0.5% albumin for 30 min. Sections were incubated with the indicated antibodies and images were acquired with a TCS SP8X White Light Laser confocal system (Leica) and a Zeiss LSM710 confocal microscope.

For whole-tissue imaging, PPs were cleared using the ScaleA2 protocol⁵⁷ for 2 weeks or Focus Clear (CelExplorer) and samples were imaged using the Zeiss Lightsheet Z.1 or LSM710 microscope. Acquired three-dimensional data stacks were reconstructed employing Imaris (Bitplane) software. Images were processed for noise removal and cells were identified as objects on the basis of the intensity of fluorescence in the respective channel, and were filtered on the basis of size.

PCR. PP total RNA was purified using the RNeasy Mini Kit (Qiagen) and cDNA was synthesized using the M-MLV Reverse Transcriptase (Promega). Real-time (RT) PCR was performed in the CFX96 Real Time System (Bio-Rad) according to the manufacturer's instructions, using the Platinum SYBR Green qPCR Mix (ThermoFisher) and with the following primers: Gp2-F 5'-CTGCTACCTCGAAGGGGACT-3'; Gp2-R 5'-CATGCCCAGAGGGAAGAAGT-3'; Spib-F 5'-GCCCACACTTAAAGCTGTTTGTGA-3'; Spib-R 5'-CTGTCCAGCCCCATGTAGAG-3'; Ccl20-F 5'-GATGGCCGATGAAGCTTGTG-3'; Ccl20-R 5'-GACTCTTAGGCTGAGGAGGTTTC-3'; Rankl-F 5'-AAACAAGCCTTTCAGGGGGG-3'; Rankl-R 5'-TCCAACCATGAGCCTTCCATC-3'; Ccl19-F 5'-CCTTAGTGTGGTGAACACAACA-3'; Ccl19-R 5'-GGGTGCTAATGATGCGGAA-3'; Ccl21-F 5'-GCTGCAAGAGAAGTGAACAGACA-3'; Ccl21-R 5'-CGTGAACCCAGCTTG-3'; Cxcl13-F 5'-TCTCTCCAGGCCACGGTATTCT-3' and Cxcl13-R 5'-ACCATTGTCACGAGGATTTCAC-3'; b2m-F 5'-TTCTGGTGTCTGCTCACTGA-3'; b2m-R 5'-CAGTATGTTCCGGCTTCCATTC-3'. Data were normalized to the housekeeping gene (*b2m*), analyzed using the 2^{- $\Delta\Delta$ CT} method, and expressed relative to control groups as indicated.

Oral immunization with cholera toxin. Mice were food-deprived for 2 h and then stomach acidity was neutralized via administration of 0.2 ml of a solution containing eight parts HBSS and two parts 7.5% sodium bicarbonate by oral gavage. After 30 min, mice were immunized by oral gavage with 30 μ g of cholera

toxin (Sigma-Aldrich). Fecal pellets were collected 7 days post immunization and analyzed by ELISA.

Murine coronavirus infections. Mice were infected orally by gavage with 5×10^8 pfu (plaque-forming units) of the murine coronavirus A59 as previously described⁷. Mice were killed and cells from small intestine lamina propria were isolated for further cytometric analysis of B cell responses and quantification of M-CoV-specific IgA antibody-secreting cells using ELISPOT.

ELISA and ELISPOT assay. Total IgA concentration in fecal samples was measured using the IgA Mouse Uncoated ELISA Kit (ThermoFisher) according to the manufacturer's instructions. Cholera toxin-coated plates in combination with the IgA Mouse Uncoated ELISA Kit were used for the detection of specific IgA.

ELISPOT assays were performed as previously described in ref.⁵⁸ using the ELISPOT kit from Mabtech. Briefly, plates were coated overnight at 4°C with 5×10^5 pfu of M-CoV A59 per well and incubated with 10^5 lamina propria cells for 24 h at 37°C in a 5% CO₂ atmosphere. Plates were washed five times with PBS and subsequently biotinylated anti-IgA secondary antibody was added for 2 h at room temperature followed by streptavidin-HRP. Spots were visualized using TMB as substrate. The enzymatic reaction was stopped by rinsing the wells with water. Plates were dried overnight and spots were counted with an ELISPOT-Reader and analyzed with the software ELISPOT 3.1SR (AID). Specific antibody-forming cells of individual mice are expressed as mean of specific spot forming cells (experimental sample – negative control) per 10^6 cells from duplicate measurements.

Commensal bacteria analysis and IgA sequencing. Analysis and isolation of IgA-coated bacteria were performed according to a previously described method^{59,60}. Fecal pellets were resuspended in PBS at 100 mg ml⁻¹ and incubated at 4°C for 20 min with shaking. After homogenization, samples were centrifuged at 50g for 15 min at 4°C and the supernatant was transferred into a new tube. Bacteria were washed three times in FACS buffer (PBS, 1% BSA and 5 mM EDTA) and pelleted at 12,000g for 1 min. Bacterial pellets were blocked with 10% rat serum for 30 min and subsequently stained with anti-mouse IgA-PE antibody for 30 min at 4°C. Samples were thoroughly washed and stained with SYTO 9 green fluorescent nucleic stain (10 μM; Life Technologies) before acquisition on a FACS ARIA III (BD).

To isolate the IgA⁺ fractions, samples were processed as above and enriched by magnetic-activated cell sorting (MACS), using anti-PE MACS beads (Miltenyi Biotec). A 10-μl aliquot of total bacteria was centrifuged before IgA enrichment for 16S rRNA sequencing analysis. The IgA⁺ fraction was further purified by FACS sorting and 5 million bacteria were collected from each sample. All bacterial samples were centrifuged and stored at 20°C for further 16S sequencing analysis.

Bacterial DNA from total and IgA-sorted fecal samples was isolated using the QIAamp UCP Pathogen Mini Kit (Qiagen) according to the manufacturer's instructions. The variable V3–V4 region of the 16S rRNA gene was amplified with universal primers and sequenced on an Illumina Miseq V3 platform (StarSEQ).

Paired-end reads were joined together using PEAR⁶¹, and any reads of insufficient quality that prevented joining were discarded (<6% of total reads). The resulting sequences were analyzed with QIIME2 v.2019.10 (ref.⁶²). Reads were corrected and amplicon sequence variants (ASVs) were obtained by the deblur workflow. Taxonomy was assigned to ASVs using a Naive-Bayes approach of the scikit learn Python library and the SILVA database⁶³. Weighted and unweighted UniFrac distances were used to visualize global differences in bacterial community compositions using PCA. For IgA index calculation and statistical analysis, data files from QIIME were analyzed in the R environment. Taxonomy was summarized to phylum, class, order, family and genus levels. A relative abundance threshold of 0.1% in either the total bacteria or the IgA⁺ fraction was used to define a certain taxon as 'present'. To define the enrichment of each detected taxon in the IgA⁺ or IgA⁻ fractions a paired Wilcoxon test was used. If a taxon was not detected in a given sample, that sample was excluded. A pseudocount (equal to 0.001, which was the lower limit of detection) was then added to every taxon detected from every sample. The differential representation of each taxon between the IgA⁺ and IgA⁻ fractions was expressed in the form of an IgA index following the formula: $\log_{10}(\text{relative abundance in the IgA}^+ \text{ fraction} / \text{relative abundance in the bulk population})$. Wilcoxon rank sum test was used to compare the magnitude of IgA response between different genotypes.

Bacterial quantitative PCR. Fecal DNA extraction and RT-PCR was performed using the reagents stated above. The abundance of specific bacterial groups was normalized with that of the total bacteria. The primers were as follows: for the total bacteria 5'-ACTCCTACGGGAGGCGAGCAGT-3' and 5'-ATTACCGGGCTGCTGGC-3'; Pseudomonas 5'-ACTTTAAGTTGGGAGGAAGGG-3' and 5'-ACACAGGAAATCCACCACCC-3'; Enterobacteria 5'-TGCCGTAACCTCGGGAGAAGGCA-3' and 5'-TCAAGGCTCAATGTTCAGTGTG-3'; Staphylococcus 5'-ACGGCTCTGTCTCACTTATA-3' and 5'-TACACATATGTTCTTCCCTAATAA-3'. Data were analyzed using the 2^{-ΔΔCT} method, and expressed relative to control groups as indicated.

Statistical analysis. Statistical analyses were performed with GraphPad Prism v.8, using one-way or two-way analysis of variance (ANOVA) unless specified otherwise. All of the statistical tests performed are indicated in the figure legends. The data are presented as mean ± s.d.

Reporting Summary. Further information on research design is available in the Nature Research Reporting Summary linked to this article.

Data availability

scRNA-seq datasets are available at ArrayExpress (accession number E-MTAB-9162). The data that support the findings of this study are available from the corresponding authors.

References

- Armaka, M. et al. Mesenchymal cell targeting by TNF as a common pathogenic principle in chronic inflammatory joint and intestinal diseases. *J. Exp. Med.* **205**, 331–337 (2008).
- Wimmer, N. et al. Lymphotoxin β receptor activation on macrophages induces cross-tolerance to TLR4 and TLR9 ligands. *J. Immunol.* **188**, 3426–3433 (2012).
- Rothe, J. et al. Mice lacking the tumour necrosis factor receptor 1 are resistant to TNF-mediated toxicity but highly susceptible to infection by *Listeria monocytogenes*. *Nature* **364**, 798–802 (1993).
- Van Hauwermeiren, F. et al. Safe TNF-based antitumor therapy following p55TNFR reduction in intestinal epithelium. *J. Clin. Invest.* **123**, 2590–2603 (2013).
- Macosko, E. Z. et al. Highly parallel genome-wide expression profiling of individual cells using nanoliter droplets. *Cell* **161**, 1202–1214 (2015).
- Zheng, G. X. et al. Massively parallel digital transcriptional profiling of single cells. *Nat. Commun.* **8**, 14049 (2017).
- McCarthy, D. J., Campbell, K. R., Lun, A. T. & Wills, Q. F. Scater: pre-processing, quality control, normalization and visualization of single-cell RNA-seq data in R. *Bioinformatics* **33**, 1179–1186 (2017).
- Stuart, T. et al. Comprehensive integration of single-cell data. *Cell* **177**, 1888–1902.e21 (2019).
- Fletcher, A. L. et al. Reproducible isolation of lymph node stromal cells reveals site-dependent differences in fibroblastic reticular cells. *Front. Immunol.* **2**, 35 (2011).
- Gil-Cruz, C. et al. Microbiota-derived peptide mimics drive lethal inflammatory cardiomyopathy. *Science* **366**, 881–886 (2019).
- Hama, H. et al. Scale: a chemical approach for fluorescence imaging and reconstruction of transparent mouse brain. *Nat. Neurosci.* **14**, 1481–1488 (2011).
- Gil-Cruz, C. et al. T helper cell- and CD40-dependent germline IgM prevents chronic virus-induced demyelinating disease. *Proc. Natl Acad. Sci. USA* **109**, 1233–1238 (2012).
- Bunker, J. J. et al. Innate and adaptive humoral responses coat distinct commensal bacteria with immunoglobulin A. *Immunity* **43**, 541–553 (2015).
- Palm, N. W. et al. Immunoglobulin A coating identifies colitogenic bacteria in inflammatory bowel disease. *Cell* **158**, 1000–1010 (2014).
- Zhang, J., Kobert, K., Flouri, T. & Stamatakis, A. PEAR: a fast and accurate Illumina Paired-End read merger. *Bioinformatics* **30**, 614–620 (2014).
- Bolyen, E. et al. Reproducible, interactive, scalable and extensible microbiome data science using QIIME 2. *Nat. Biotechnol.* **37**, 852–857 (2019).
- Quast, C. et al. The SILVA ribosomal RNA gene database project: improved data processing and web-based tools. *Nucleic Acids Res.* **41**, D590–D596 (2013).

Acknowledgements

The authors thank M. Meletiou and S. Lalos for technical assistance in mouse genotyping and histology. We thank K. Dagla and S. Grammenoudi for assistance in flow cytometry. The authors acknowledge support of this work by the InfrafrontierGR Infrastructure, cofunded by Greece and the European Union (European Regional Development Fund) under NSRF 2014–2020, MIS 5002135, which provided mouse housing, transgenesis and phenotyping facilities, histopathology, flow cytometry and advanced microscopy facilities. This work was supported by the FP7 Advanced ERC Grant MCs-inTEST (grant no. 340217) to G.K. and the Swiss National Science Foundation (grant nos 166500 and 182583) to B.L.

Author contributions

A.P. and L.O. designed and performed experiments, analyzed and interpreted data and wrote the manuscript. H.-W.C., U.M., C.G.-C. and C.P.-S. performed experiments. M.L. analyzed data. V.K. analyzed and interpreted data and wrote the manuscript. B.L. and G.K. conceived and designed the study, discussed the data and wrote the manuscript.

Competing interests

B.L., L.O., C.G.-C., C.P.-S. and H.-W.C. are cofounders and shareholders of Stromal Therapeutics AG. H.-W.C. is a part-time employee of Stromal Therapeutics AG. There are no competing interests to report for the remaining co-authors.

Additional information

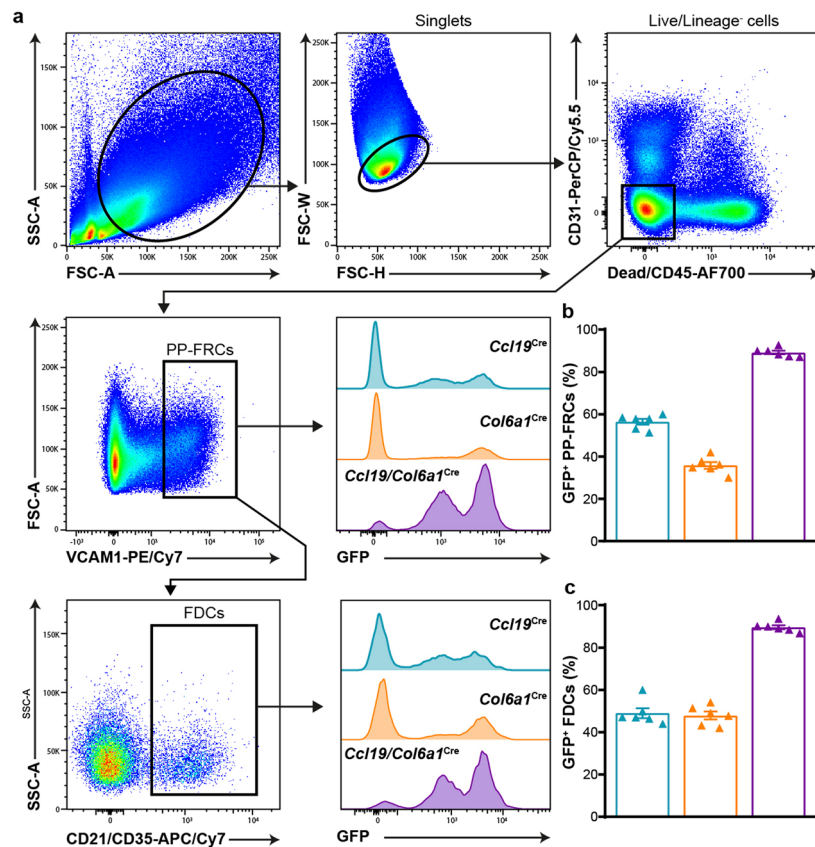
Extended data is available for this paper at <https://doi.org/10.1038/s41590-021-00894-5>.

Supplementary information The online version contains supplementary material available at <https://doi.org/10.1038/s41590-021-00894-5>.

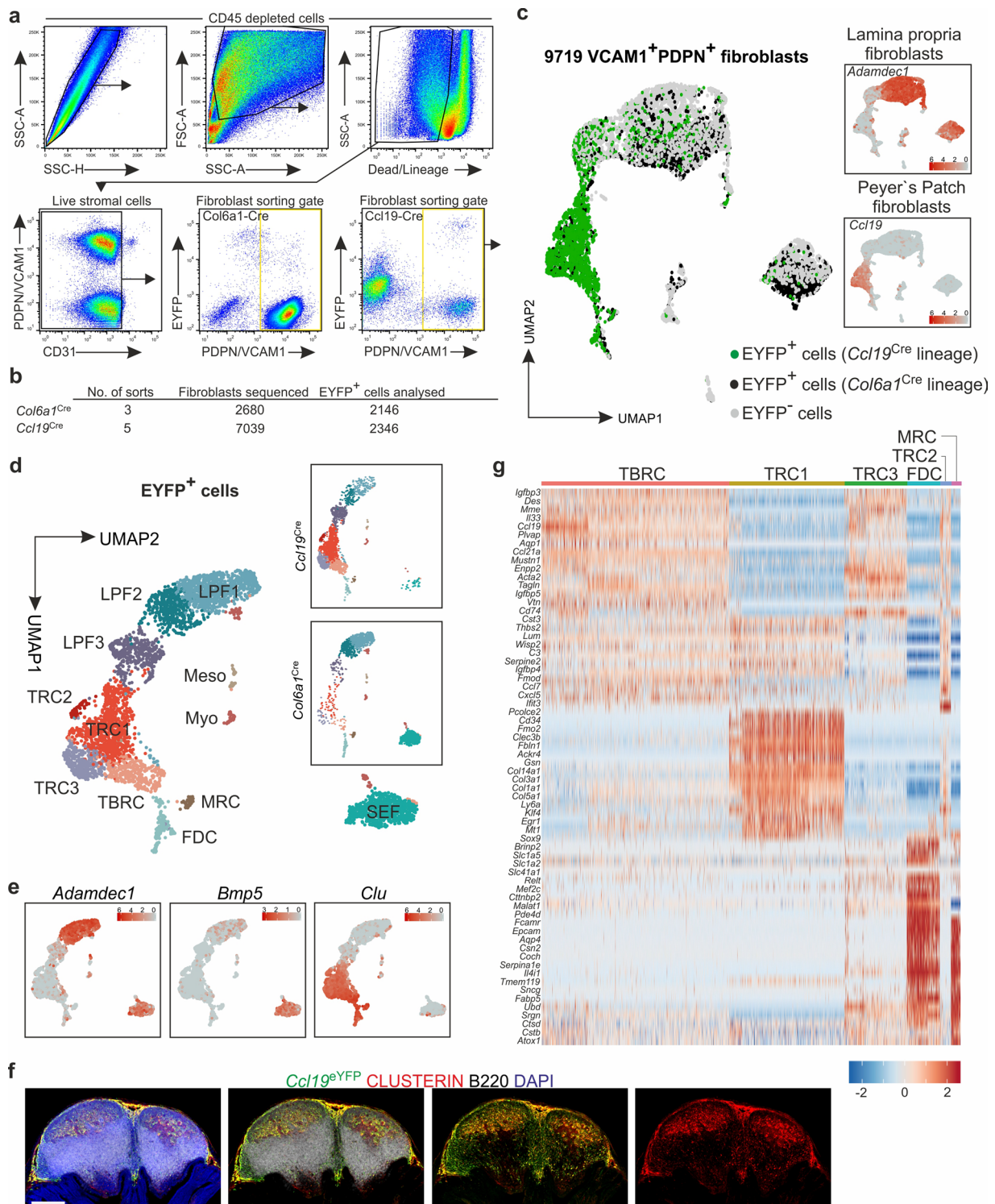
Correspondence and requests for materials should be addressed to B.L. or G.K.

Peer review information *Nature Immunology* thanks Michael Carroll and the other, anonymous, reviewer(s) for their contribution to the peer review of this work. L. A. Dempsey was the primary editor on this article and managed its editorial process and peer review in collaboration with the rest of the editorial team.

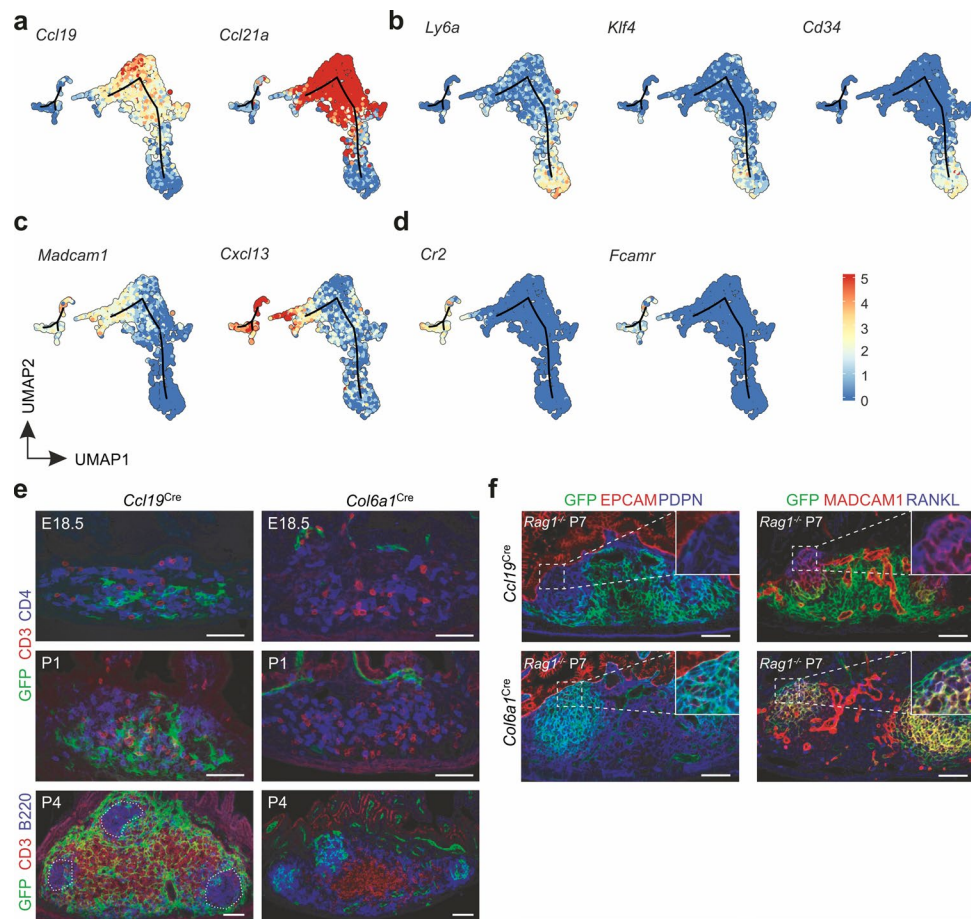
Reprints and permissions information is available at www.nature.com/reprints.



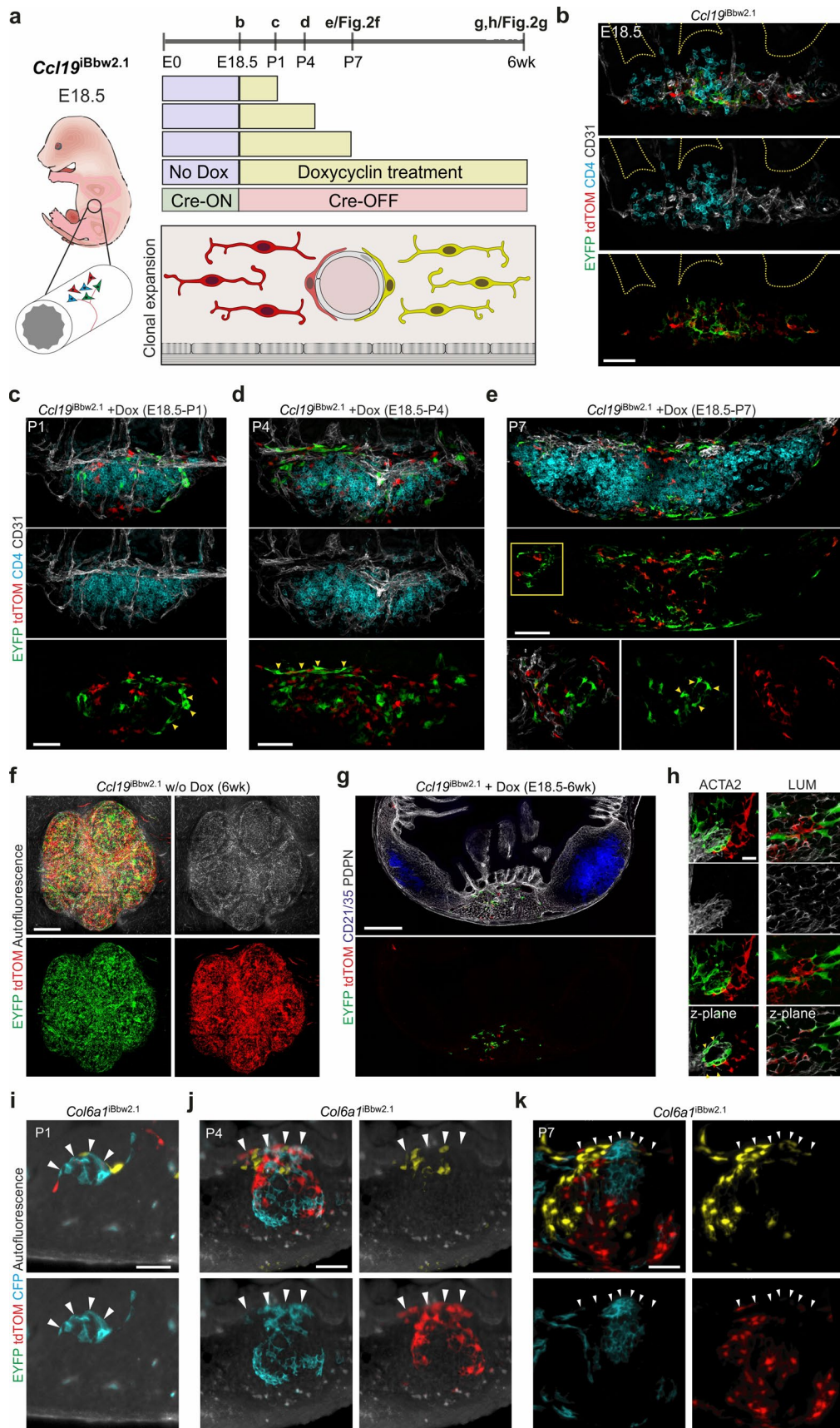
Extended Data Fig. 1 | Flow cytometry analysis of PP-FRC and FDC targeting by the *Ccl19*^{Cre} and *Col6a1*^{Cre} strains. **a, FACS gating strategy used to analyze Cre-mediated GFP expression in PP-FRCs (live CD31-CD45-VCAM1^{hi} cells) and CD21/CD35⁺ FDCs from *Ccl19*^{Cre} R26^{mTmG}, *Col6a1*^{Cre} R26^{mTmG} and *Ccl19/Col6a1*^{Cre} R26^{mTmG} mice. **b-c**, Bar plot shows the proportion of targeted total FRCs (**b**) and FDCs (**c**) in these mice (n = 6 mice/genotype). Mean percentages and SD are indicated.**



Extended Data Fig. 2 | Single cell RNA-sequencing analysis of PP FRC. **a**, Flow cytometry based sorting strategy for PDPN⁺VCAM1⁺ fibroblasts from adult *Ccl19^{eYFP}* and *Col6a1^{eYFP}* PPs. **b**, Statistics for cell sorting and scRNA sequencing. **c**, UMAPs showing all fibroblasts sequenced, after removal of contaminating cells (see Materials and Methods). Highlighted are EYFP-expressing cells from the two different Cre driver lines, small UMAPs show gene expression to determine *Adamdect1*⁺ lamina propria fibroblasts (LPF) and *Ccl19*⁺ PP FRCs. **d**, UMAPs displaying 12 clusters of re-embedded EYFP⁺ fibroblasts and the contribution of the two Cre driver lines is shown in the boxed split UMAPs. **e**, Gene expression feature UMAPs showing *Adamdect1* expression to determine lamina propria fibroblasts, *Bmp5* to determine subepithelial fibroblasts (SEF) and *Clu* for the identification of PP FRCs among EYFP expressing cells. **f**, Images showing PP from adult *Ccl19^{eYFP}* mice. **g**, Heatmap displaying top marker gene expression of individual cells for each PP FRC cluster. Meso (Mesothelial cells), Myo (Myocytes); Scale bar, 500 μ m. Images are representative of 3 mice. ScRNA-sequencing data represents 9719 fibroblasts (c) or 4492 EYFP⁺ fibroblasts (d), 8 biological replicates, 4 independent experiments.

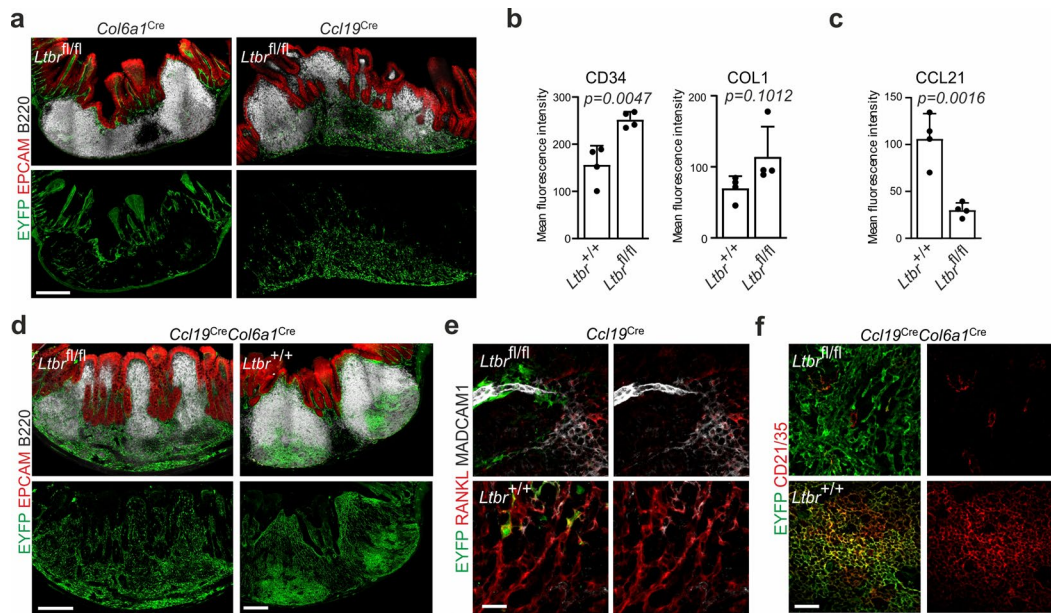


Extended Data Fig. 3 | Differentiation trajectories of PP FRC. Gene expression levels of **a**, *Ccl19* and *Ccl21a*; **b**, *Ly6a*, *Klf4* and *Cd34*; **c**, *Madcam1* and *Cxcl13*; **d**, *Cr2* and *Fcaml*; **e**, Images showing PP anlagen at E18.5, P1 and P4 harvested from *Ccl19^{eYFP}* and *Col6a1^{eYFP}* mice. **f**, Images showing PP at P7 harvested from *Rag^{KO}Ccl19^{eYFP}* and *Rag^{KO}Col6a1^{eYFP}* mice. Boxes indicate subepithelial region. Scale bars, 50 μm (**e,f**). Images are representative of at least 3 mice from 2-4 independent experiments. Monocle analysis is based on scRNA-sequencing data in Fig. 1c, N = 8 biological replicates, 4 independent experiments.

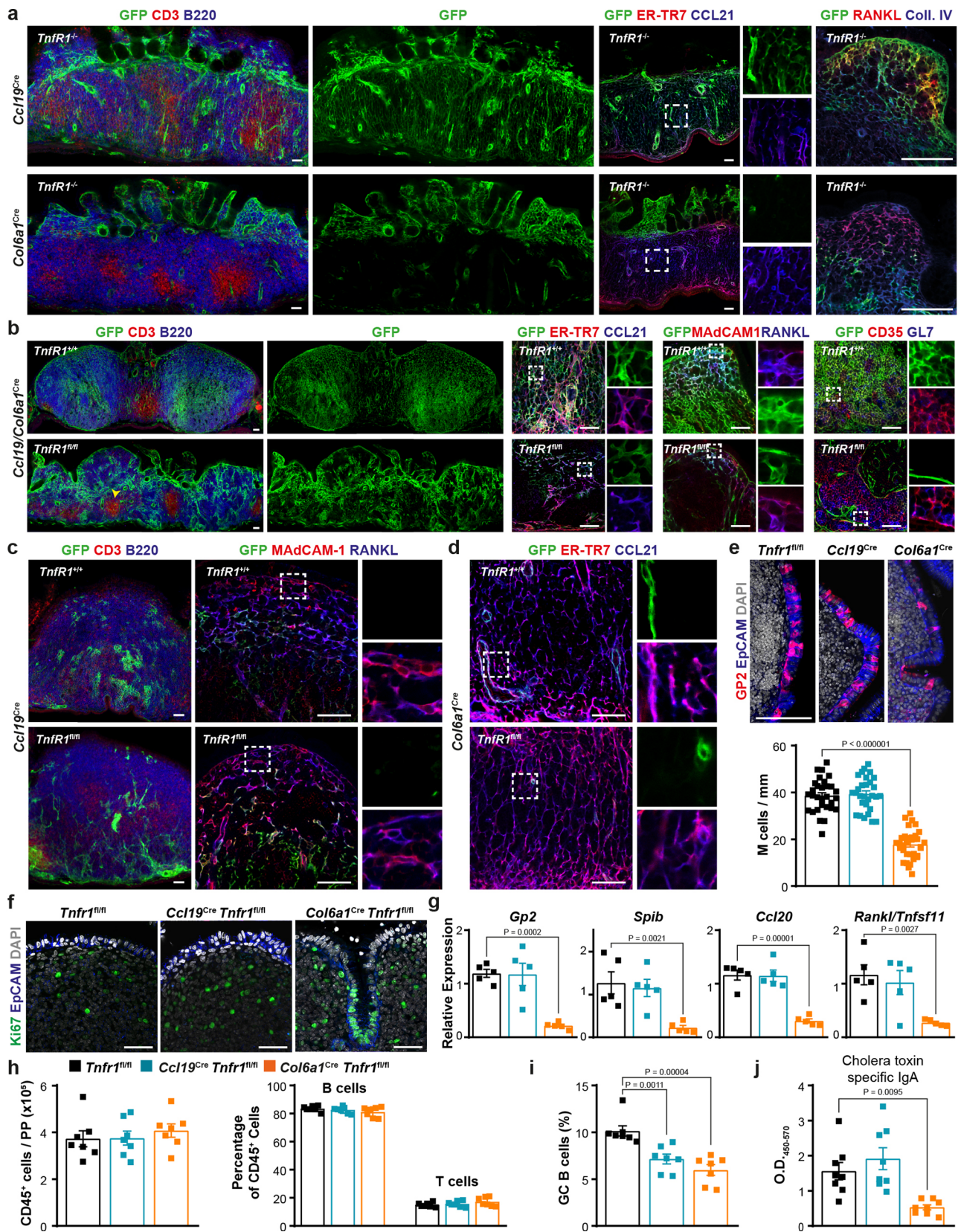


Extended Data Fig. 4 | See next page for caption.

Extended Data Fig. 4 | Fate-mapping of lymphoid tissue organizer cells. **a**, Schematic description of fate-mapping experiments in *Ccl19*^{ibbw2.1} mice. Pregnant mice were treated with Doxycyclin (Dox) at embryonic day (E) 18.5 and offsprings were analysed at indicated timepoints. **b**, Images showing PP anlage at E18.5 harvested from *Ccl19*^{ibbw2.1} embryos. Dashed line indicates intestinal epithelium. **c**, Images showing PP anlagen at postnatal day (P) 1 and P4 (in **d**) harvested from *Ccl19*^{ibbw2.1} pups kept on Dox since E18.5. Arrowheads indicate perivascular EYFP⁺ cell cluster. **e**, Images showing PP anlage at P7 harvested from *Ccl19*^{ibbw2.1} pups kept on Dox since E18.5. Boxed area indicates representative area of higher magnification images below, Arrowheads indicate EYFP⁺ cell cluster. **f**, Images show whole-mount analysis of adult PP from *Ccl19*^{ibbw2.1} mice, which were kept without (w/o) Dox. **g**, Images depicting histological section of adult PP harvested from *Ccl19*^{ibbw2.1} mice kept on doxycycline since E18.5. **h**, Images showing high resolution confocal analysis of EYFP⁺ and tdTOMATO⁺ cell clusters in PP from adult *Ccl19*^{ibbw2.1} mice kept on Dox since E18.5. Scale bars, 20 μm (**b,c**), 50 μm (**d**), 100 μm (**e**), 500 μm (**f,g**), 10 μm (**h**). Images are representative of at least 3 mice from 2-3 independent experiments.

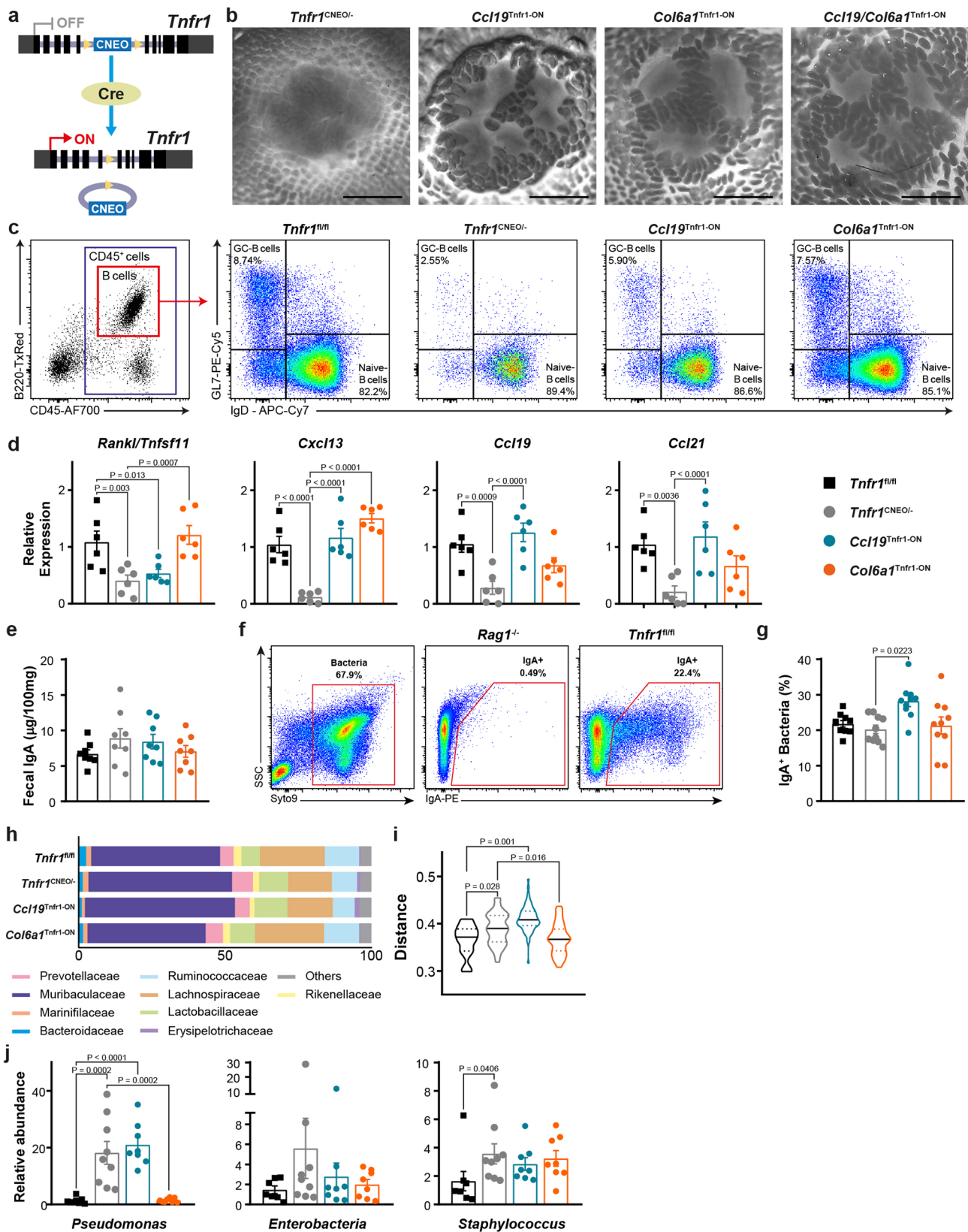


Extended Data Fig. 5 | Peyer's Patch structure in *Ltbr* conditional knock out mice. **a**, Microscopy images showing PP of adult mice conditionally ablated for *Ltbr* in indicated Cre mouse lines. **b-c**, Mean fluorescence intensity analysis of indicated markers enumerated from microscopy images of adult *Ccl19^{eYFP}Ltbr^{+/+}* and *Ccl19^{eYFP}Ltbr^{fl/fl}* PPs ($n=4$ mice per group). **d**, Confocal microscope images showing sections of adult *Ccl19^{eYFP}Col6a1^{eYFP}Ltbr^{fl/fl}* and *Ccl19^{eYFP}Col6a1^{eYFP}Ltbr^{+/+}* PPs. **e**, Images show EYFP⁺RANKL⁺MADCAM1⁺ MRC networks in PPs of indicated adult mice. **f**, Images show EYFP⁺CD21/35⁺ FDC networks in PPs of indicated adult mice. Scale bars, 500 μm (a,d), 20 μm (e,f). Images are representative of 3-5 mice from 2 independent experiments. (b,c) Mean percentages and SD are indicated; P values as per two-sided Student's t -test.



Extended Data Fig. 6 | See next page for caption.

Extended Data Fig. 6 | Peyer's Patch structure of *Tnfr1*^{-/-} and *Tnfr1* conditional knock out mice. **a**, Confocal microscopy images display the topology of *Ccl19*^{Cre} and *Col6a1*^{Cre} lineages in *Tnfr1*^{-/-} PPs (n=5 mice per group). **b**, Confocal microscopy analysis of adult PPs from *Ccl19/Col6a1*^{Cre} *Tnfr1*^{fl/fl} mice. The arrowhead shows the presence of T cell aggregates under an epithelial dome of *Ccl19/Col6a1*^{Cre} *Tnfr1*^{fl/fl} PPs. **c**, Images showing the B cell area (left) and the MRC network in *Ccl19*^{Cre} *Tnfr1*^{+/+} and *Tnfr1*^{fl/fl} mice. **d**, Confocal images showing TRC networks in *Col6a1*^{Cre} *Tnfr1*^{+/+} and *Tnfr1*^{fl/fl} mice. **e-f**, Confocal microscope analysis showing GP2⁺ M cells and Ki67⁺ proliferating cells in the epithelial dome of adult *Tnfr1*^{fl/fl}, *Ccl19*^{Cre} *Tnfr1*^{fl/fl}, *Col6a1*^{Cre} *Tnfr1*^{fl/fl} PPs. M cells were quantified in PP follicles from 5 mice per group. **g**, Relative expression of *Gp2*, *Spib*, *Ccl20* and *Tnfsf11* in whole PPs measured by real-time PCR (n=5 mice/genotype). **h-i**, Flow cytometric analyses characterizing the absolute numbers of CD45⁺ cells, and the proportion of B cells, T cells GC-B cells in PPs (n = 7 mice/genotype). **j**, ELISA of cholera toxin-specific IgA response. Mice were orally immunized with cholera toxin 1 week before the examination (n=8 mice/genotype). Scale bars, 50 μm. Images are representative of 5 mice per group, at least 3 independent experiments. *P* values as one-way ANOVA (**e,g,h-j**). Mean percentages and SEM are indicated.



Extended Data Fig. 7 | See next page for caption.

Extended Data Fig. 7 | Structural and functional analysis of *Tnfr1* reactivation in PP-FRCs. **a**, Schematic description of *Tnfr1*^{creo} model. **b**, PP stereoscope images from adult *Tnfr1*^{creo/-}, *Ccl19*^{Tnfr1-ON}, *Col6a1*^{Tnfr1-ON} and *Ccl19/Col6a1*^{Tnfr1-ON} mice. Scale bar = 1mm. **c**, Gating strategy used in Fig. 4d,i. **d**, Relative expression of *Rankl/Tnfsf11*, *Cxcl13*, *Ccl19* and *Ccl21* in FACS sorted PP-FRCs, measured by real-time PCR (n = 6 mice/genotype) **e**, Fecal IgA concentration measured by ELISA (n = 8 mice/genotype). **f**, Representative flow cytometry plots of IgA-coated bacteria. *Rag1*^{-/-} mice were used as a negative control. **g**, Frequencies of fecal IgA-coated bacteria in the indicated genotypes (n = 8 mice/genotype). **h**, Quantification of bacterial families with a relative abundance >1% in fecal samples. **i**, Unweighted UniFrac analysis for total fecal bacteria samples (*Tnfr1*^{fl/fl} n=8, *Tnfr1*^{creo/-} n=9, *Ccl19*^{Tnfr1-ON} n=8 and *Col6a1*^{Tnfr1-ON} n=8). **j**, Relative abundance of *Pseudomonas*, *Enterobacteria* and *Staphylococcus* in fecal samples measured by qPCR (*Tnfr1*^{fl/fl} n=8, *Tnfr1*^{creo/-} n=9, *Ccl19*^{Tnfr1-ON} n=8 and *Col6a1*^{Tnfr1-ON} n=8). P value as one-way ANOVA (**d,e,g,j**). Mean and SEM are indicated.

Reporting Summary

Nature Research wishes to improve the reproducibility of the work that we publish. This form provides structure for consistency and transparency in reporting. For further information on Nature Research policies, see our [Editorial Policies](#) and the [Editorial Policy Checklist](#).

Statistics

For all statistical analyses, confirm that the following items are present in the figure legend, table legend, main text, or Methods section.

n/a Confirmed

- The exact sample size (n) for each experimental group/condition, given as a discrete number and unit of measurement
- A statement on whether measurements were taken from distinct samples or whether the same sample was measured repeatedly
- The statistical test(s) used AND whether they are one- or two-sided
Only common tests should be described solely by name; describe more complex techniques in the Methods section.
- A description of all covariates tested
- A description of any assumptions or corrections, such as tests of normality and adjustment for multiple comparisons
- A full description of the statistical parameters including central tendency (e.g. means) or other basic estimates (e.g. regression coefficient) AND variation (e.g. standard deviation) or associated estimates of uncertainty (e.g. confidence intervals)
- For null hypothesis testing, the test statistic (e.g. F , t , r) with confidence intervals, effect sizes, degrees of freedom and P value noted
Give P values as exact values whenever suitable.
- For Bayesian analysis, information on the choice of priors and Markov chain Monte Carlo settings
- For hierarchical and complex designs, identification of the appropriate level for tests and full reporting of outcomes
- Estimates of effect sizes (e.g. Cohen's d , Pearson's r), indicating how they were calculated

Our web collection on [statistics for biologists](#) contains articles on many of the points above.

Software and code

Policy information about [availability of computer code](#)

Data collection FACSDiva (BD Biosciences, v8.0.1), FACSort (BD Biosciences, v1.3.3), ProSort (Bio-Rad, v9.1) Zen (Zeiss, v14.018.201 and v2014 SP1), Leica LAS-AF (v3.3.0)

Data analysis FlowJo (Treestar Inc., V10), Graphpad (Prism v8), CellRanger (v3.0.1), R Studio (v3.6.0 and v3.6.2), Seurat package (v3.1.1) R/Bioconductor package (v1.11.2), Monocle 3 analysis toolkit (v0.2.0), QIIME2 (v2019), Imaris (v8), ELISPOT 3.1SR.

For manuscripts utilizing custom algorithms or software that are central to the research but not yet described in published literature, software must be made available to editors and reviewers. We strongly encourage code deposition in a community repository (e.g. GitHub). See the Nature Research [guidelines for submitting code & software](#) for further information.

Data

Policy information about [availability of data](#)

All manuscripts must include a [data availability statement](#). This statement should provide the following information, where applicable:

- Accession codes, unique identifiers, or web links for publicly available datasets
- A list of figures that have associated raw data
- A description of any restrictions on data availability

The data that support will be available from the corresponding authors upon request.

Field-specific reporting

Please select the one below that is the best fit for your research. If you are not sure, read the appropriate sections before making your selection.

Life sciences Behavioural & social sciences Ecological, evolutionary & environmental sciences

For a reference copy of the document with all sections, see [nature.com/documents/nr-reporting-summary-flat.pdf](https://www.nature.com/documents/nr-reporting-summary-flat.pdf)

Life sciences study design

All studies must disclose on these points even when the disclosure is negative.

Sample size	No sample-size calculation was performed; sample sizes were determined to be adequate based on the reproducibility between independent experiments.
Data exclusions	No data points were excluded.
Replication	Experiments were repeated at least three times and with sufficient animals per group to demonstrate statistical significance. All experiments were reliable reproduced.
Randomization	Animals were randomly allocated for examination.
Blinding	Blinding was not performed since data analysis was strictly quantitative and not subjective.

Reporting for specific materials, systems and methods

We require information from authors about some types of materials, experimental systems and methods used in many studies. Here, indicate whether each material, system or method listed is relevant to your study. If you are not sure if a list item applies to your research, read the appropriate section before selecting a response.

Materials & experimental systems

n/a	Involved in the study
<input type="checkbox"/>	<input checked="" type="checkbox"/> Antibodies
<input checked="" type="checkbox"/>	<input type="checkbox"/> Eukaryotic cell lines
<input checked="" type="checkbox"/>	<input type="checkbox"/> Palaeontology and archaeology
<input type="checkbox"/>	<input checked="" type="checkbox"/> Animals and other organisms
<input checked="" type="checkbox"/>	<input type="checkbox"/> Human research participants
<input checked="" type="checkbox"/>	<input type="checkbox"/> Clinical data
<input checked="" type="checkbox"/>	<input type="checkbox"/> Dual use research of concern

Methods

n/a	Involved in the study
<input checked="" type="checkbox"/>	<input type="checkbox"/> ChIP-seq
<input type="checkbox"/>	<input checked="" type="checkbox"/> Flow cytometry
<input checked="" type="checkbox"/>	<input type="checkbox"/> MRI-based neuroimaging

Antibodies

Antibodies used

Anti-CD3 (17A2, AF594, 100240), anti-CD21/CD35 (7E9, APC-Cy7, 123418), anti-CD31 (390, PerCP-Cy5.5, 102420), anti-CD45 (30-F11, AF700, 103128), anti-B220 (RA3-6B2, biotin, 103204), anti-IgD (11-26c.2a, APC-Cy7, 405716), anti-MAdCAM-1 (MECA-367, purified, 120702; MECA-367, biotin, 120706) and anti-VCAM-1 (429, PE-Cy7, 105720) were purchased from Biolegend; anti-aSMA (1A4, eFluor660, 50-9760-82), anti-CD3e (145-2C11, PE-Cy7, 25-0031-82), anti-CD4 (RM4-5, AF700, 56-0042-82), anti-EpCAM (G8.8, purified, 14-5791-81), anti-GL7 (GL7, biotin, 13-5902-82), anti-IgA (mA-6E1, PE, 12-4204-82), anti-podoplanin (eBio8.1.1, eFluor660, 50-5381-82), anti-CD34 (RAM34, biotin, 13-0341-82) and anti-RANKL (1K22/5, biotin, 13-5952-82) were purchased from Thermo Fisher; anti-CD31 (MEC13.3, purified, 550274), anti-CD35 (8C12, purified, 558768), anti-B220 (RA3-6B2, PE-CF594, 562290) were purchased from BD Pharmingen; anti-CCL21 (biotin, BAF457) was purchased from R&D Systems; anti-GP2 (2F11-C3, biotin, D278-6) was purchased from MBL; anti-collagen IV (purified, ab6586) and anti-ER-TR7 (purified, ab51824) were purchased from Abcam; anti-YFP (purified, 632459) and anti-TOMATO (purified, 632496) were purchased from Takara. Anti-M-CoV-NP (J3.3, purified, kindly provided by S. Siddell, University of Würzburg, Germany). Unconjugated antibodies were detected with the following secondary antibodies: Alexa Fluor 594-conjugated goat anti-rat-IgG (A11007), Alexa Fluor 594-conjugated goat anti-rabbit-IgG (A-11012), Alexa Fluor 647-conjugated goat anti-rat-IgG (A21247) all purchased from Thermo Fisher. Biotinylated antibodies were detected using AF647-Streptavidin (S21374) from Thermo Fisher, and PE-Cy5- (554062) or APC-Streptavidin (554067) from BD Pharmingen. RANKL and CCL21 expression were detected using the Tyramide SuperBoost Kit (Thermo Fisher, B40936).

Validation

All antibodies except anti-M-CoV-NP (J3.3) came from commercial vendors, and were validated by the manufacturers on their official website.

Animals and other organisms

Policy information about [studies involving animals](#); [ARRIVE guidelines](#) recommended for reporting animal research

Laboratory animals	We use laboratory mice (<i>Mus musculus</i>) from C57BL/6 background between 6 and 12 weeks of age. Both females and males were included in the study.
Wild animals	None
Field-collected samples	None
Ethics oversight	Experiments were performed in accordance with all current European and national legislation and were approved by the Institutional Committee of Protocol Evaluation in conjunction with the Veterinary Service Management of the Hellenic Republic Prefecture of Attika under the permissions 5759/15, 1989/19, 213088/19 and the Swiss federal and cantonal guidelines (Tierschutzgesetz) under the permissions SG01/18, SG12/17, SG08/18 and SG11/19 granted by the Veterinary Office of the Kanton of St. Gallen.

Note that full information on the approval of the study protocol must also be provided in the manuscript.

Flow Cytometry

Plots

Confirm that:

- The axis labels state the marker and fluorochrome used (e.g. CD4-FITC).
- The axis scales are clearly visible. Include numbers along axes only for bottom left plot of group (a 'group' is an analysis of identical markers).
- All plots are contour plots with outliers or pseudocolor plots.
- A numerical value for number of cells or percentage (with statistics) is provided.

Methodology

Sample preparation	A description of the sample preparation for the flow cytometry is detailed in the methods section.
Instrument	Biorad S3 (Biorad), BD FACSMelody, BD FACSCanto, BD FACSAria II BD.
Software	FACSDiva was used to collect data and FlowJo to analyze data. For cell sorting for scRNA-Seq, ProSort S3 and FACS Chorus was used to set up cell sorting. FACS Aria II was used for bacteria sorting for IgA-sequencing.
Cell population abundance	A test sample was prepared for testing the purity of sorted cells. While acquiring data for cellular phenotyping, at least 5000-10000 cells were included in the stopping gate.
Gating strategy	All analysis begin with Cells (SSC-A vs FSC-A) > singlets (FSC-A vs FSC-H) > Live cells. For FRC analysis, cells were gated as CD45-, CD31- and VCAM1 positive events. FDCs were gated as CD35+ FRCs. GC-B cell were identified as CD45+, B220+, GL7+, IgD- cells and T cells as CD45+ CD3+ events.

- Tick this box to confirm that a figure exemplifying the gating strategy is provided in the Supplementary Information.